

Photonic quantum signatures of chaos and boson sampling

V. M. Bastidas,^{1,*} H. L. Nourse,^{2,†} A. Sakurai,² A. Hayashi,^{2,3,4} S. Nishio,^{2,3,4} Kae Nemoto,^{2,3,4} and W. J. Munro^{1,4}

¹*NTT Basic Research Laboratories & Research Center for Theoretical Quantum Physics, 3-1 Morinosato-Wakamiya, Atsugi, Kanagawa, 243-0198, Japan*

²*Quantum Information Science and Technology Unit, Okinawa Institute of Science and Technology Graduate University, Onna-son, Okinawa 904-0495, Japan*

³*School of Multidisciplinary Science, Department of Informatics, SOKENDAI (the Graduate University for Advanced Studies), 2-1-2 Hitotsubashi, Chiyoda-ku, Tokyo 101-8430, Japan*

⁴*National Institute of Informatics, 2-1-2 Hitotsubashi, Chiyoda-ku, Tokyo 101-8430, Japan*

(Dated: August 2, 2023)

Boson sampling is a paradigmatic example of a task that can be performed by a quantum photonic computer yet is hard for digital classical computers. In a typical boson sampling experiment, the scattering amplitude is determined by the permanent of a submatrix of a unitary drawn from an ensemble of random matrices. Random matrix theory plays a very important role in quite diverse fields while at the same time being intimately related to quantum signatures of chaos. Within this framework, a chaotic quantum system exhibits level statistics characteristic of ensembles of random matrices. Such quantum signatures are encoded in the unitary evolution and so in this work we combine the dynamics of chaotic systems with boson sampling. One of the key results of our work is that we demonstrate the intimate relation between out-of-time-order correlators and boson sampling. We show that the unitary dynamics of a Floquet system may be exploited to perform sampling tasks with identical particles using single-mode phase shifters and multipoint beamsplitters. At the end of our paper propose a photonic implementation of the multiparticle kicked rotor, which provides a concrete example of our general approach.

I. INTRODUCTION

The interplay between chaos and complexity plays an important role in our daily life and especially in technological applications [1, 2]. Classically chaotic systems are well known to be extremely sensitive to small perturbations in the parameters that define them [3, 4]. The exploration of these systems is challenging and their importance in our lives is evident from the prediction of the weather forecast [5], the study of turbulence [6] and fluid dynamics to the behavior of financial markets [7]. Of course, such behavior is not restricted to classical systems.

In the quantum world there are complex systems that exhibit a well-defined semiclassical limit that is chaotic in nature [8–10]. The investigation of the properties of these quantum systems is not simple because far away from the semiclassical limit the notion of phase-space trajectories is not well defined and one needs to look for quantum manifestations of chaotic behavior [9, 11]. These manifestations are referred to as quantum signatures of chaos (QSOC) [9, 11–14] and currently there is a plethora of them, ranging from level statistics [10, 15, 16], Loehschmidt echoes [17, 18], out-of-time order correlators [13, 19–21], and information scrambling [22–25]. In the context of level statistics, it is conjectured [26–29] that the spectral properties of a system with a chaotic semiclassical limit are related to random matrix theory (RMT) and the symmetries of the system [30–32]. Experimental demonstrations of QSOC are abundant in diverse communities such as nuclear physics [31], cold atoms [33, 34], trapped ions [35] and superconducting qubits [36, 37].

Complexity in manybody quantum systems can also appear due to the statistics of the particles, even if they are not interacting [38–40]. Perhaps the most intriguing example of this is the problem of boson sampling [41–43]. In this context, to sample the output of multiple bosonic particles in a given number of modes turns out to be hard for digital classical computers [41]. The underlying reason for this is the multiparticle interference of bosonic particles [44, 45], resulting in the output of a sampling experiment given in terms permanent [41], which is hard to compute. In the complexity proof for boson sampling there is an intriguing connection to RMT [41]. In approximate sampling, it is usually assumed that the single-particle unitary determining the behavior of each boson is chosen according to the Haar measure [43, 46, 47]. Hence, the transition probability between a given input and the desired output is determined by the permanent of a submatrix of a random unitary [41]. As a consequence, for the boson sampling task to be hard the submatrices satisfy the sufficient condition that its elements are i.i.d. complex random Gaussian variables [41].

This suggests that there may be an intriguing link between systems that exhibit QSOC and boson sampling. It is natural to ask whether one can exploit the complexity of a single-particle system that is chaotic to perform boson sampling in the case of multiple bosonic particles. This is a priori a nontrivial question as the complex behavior may originate from two different sources. One of them is the single-particle chaotic behavior. Recent works have proposed to use quantum control to effectively simulate the dynamics of a unitary chosen from the Haar measure [48] and discussed the intimate relation between dynamical phase transition in sampling complexity and the time evolution generated by spatially local quadratic bosonic Hamiltonians [49].

In this work, we establish the relation between QSOC and

* victor.bastidas@ntt.com; These authors contributed equally to this work.

† These authors contributed equally to this work.

boson sampling. We discuss QSOC for general photonic systems of non-interacting photons such as level statistics, spectral form factors (SFF), and localization properties of Floquet states. With these results at hand, we define a photonic out-of-time-order correlator (OTOC) and show that it is related to the output of a boson sampling experiment, which is a key result of our work. We explore how the dynamics are intimately related to the crossover from regular to chaotic behavior at the single-particle level. To substantiate our results, we propose a photonic implementation of the kicked rotor, a paradigmatic model in the community of quantum chaos [50–56]. Our proposed photonic system is given as a product of phase shifters and a multiport beam splitter [57]. We also consider the effect of disorder in the phase shifters. Both the strengths of the disorder and the multiport beam splitters control the crossover from regular to chaotic behavior, allowing the exploration of a wide parameter space.

Now in Fig. 1 we show a schematic that illustrates the main idea of our work. The intimate relation between QSOC and random matrix theory (RMT) tell us that chaotic systems show universality [8, 9], and are described by ensembles of random matrices such as the Gaussian orthogonal ensemble (GOE) or the Circular orthogonal ensemble COE [31]. We show that the ability of the system to explore the available configurations over time might be related to the complexity of the sampling problem. When the system is in the regular regime, it can explore most of the available configurations. In contrast, when the system is in the chaotic regime, it can only access a few of them. We show numerical evidence that for the kicked rotor in the chaotic regime the corresponding unitary, with GOE spectral statistics, has submatrices that are a random Gaussian, which is a sufficient condition for boson sampling to be hard [41].

The structure of our paper is as follows. In Section II we provide a brief summary of the basic aspects of Floquet theory and boson sampling. Then in Section III we introduce QSOC, such as quasienergy level statistics, spectral form factors, and localization properties of Floquet states. Next in Section IV we show one of our key results relating photonic OTOCs with boson sampling. In Section V we discuss how QSOC influence the dynamics of local observables and, in particular, we discuss the relation to equilibration. Then in Section VI we provide an intuitive explanation of the relation between QSOC and the complexity of boson sampling, which is another key result of our work. The results presented in the aforementioned sections are general. For this reason in Section VII, we provide a specific example of a photonic Floquet system exhibiting QSOC, that is intimately related to the kicked rotor. For this particular example, in Section VIII we present numerical results for QSOC, dynamics of observables measurable in experiments and the statistics of submatrices. Lastly, we provide concluding remarks and an outlook in Section IX.

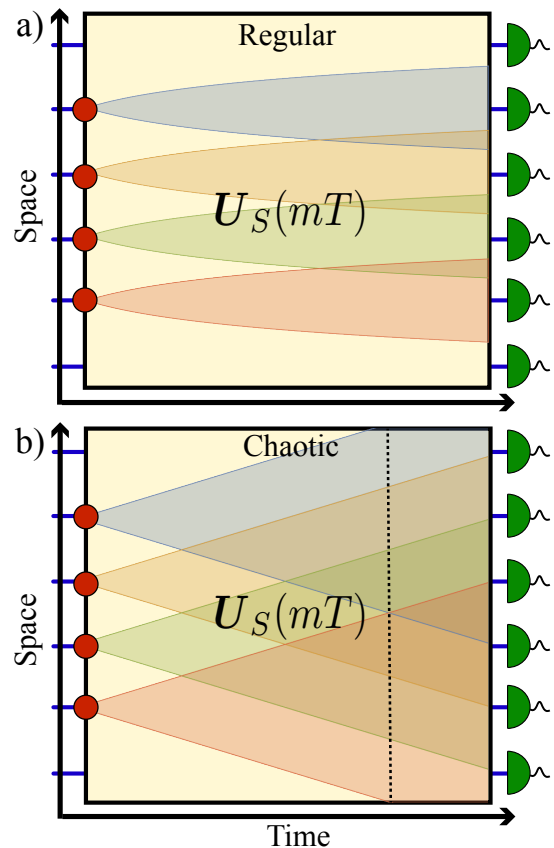


FIG. 1. Schematic illustration of the main idea of our work: boson sampling with regular vs chaotic Floquet dynamics. In boson sampling, the dynamics of the modes are generated by an $M \times M$ unitary matrix $U_S(mT)$, where M is the number of modes and T is the period. a) When the dynamics are regular, the photons remain localized with restricted operator spreading (shaded areas) and not all of them are able to interfere. b) In the chaotic regime, the operators spread with a typical linear light cone (shaded areas). This allows all the photons to effectively interfere after a characteristic time (dashed line). Due to causality, identical photons can only interfere when their lightcones overlap. This interference is the underlying mechanism that allows equilibration of local observables at long times.

II. PERIODIC PHOTONIC CIRCUITS: FLOQUET THEORY AND BOSON SAMPLING

In our work we will establish a general framework that exploits photonic dynamics and QSOC to perform boson sampling. We will extensively use tools of periodically-driven systems theory [58]. Let us start by examining the photonic dynamics in the context of Floquet theory for time-periodic Hamiltonians $\hat{H}(t+T) = \hat{H}(t)$ with a period T [58]. Due to the time-periodicity, it is convenient to define the Floquet operator $\hat{\mathcal{F}} = \hat{U}(T)$ that generates the evolution of the system $|\Psi(mT)\rangle = \hat{\mathcal{F}}^m |\Psi(0)\rangle$ at stroboscopic times $t_m = mT$.

The advantage of using the language of Floquet theory is that we can use many results of periodically driven quantum systems to understand properties of the photonic system. In an actual photonic implementation, the coaxial propagation

coordinate z of light along an optical waveguide acts as a ‘‘time’’ [59]. From now on, we will keep this in mind when we talk about time in our work.

Next, let us explore to which extent Floquet theory relates to boson sampling. We will consider the initial state

$$|\Psi(0)\rangle = |n_1^{(I)}, n_2^{(I)}, \dots, n_M^{(I)}\rangle = \prod_{j=1}^M \frac{(\hat{a}_j^\dagger)^{n_j^{(I)}}}{[n_j^{(I)}!]^{1/2}} |\mathbf{0}\rangle, \quad (1)$$

where $|\mathbf{0}\rangle = |0_1, 0_2, \dots, 0_M\rangle$ represents the vacuum. Eq. (1) describes an initial configuration I of $N = \sum_j n_j^{(I)}$ particles distributed among M modes, where $n_j^{(I)}$ is the number of photons in mode j . For simplicity we restrict ourselves to an initial configuration where at most one particle can occupy a given mode ($n_j^{(I)} \in \{0, 1\}$). We denote the single-particle basis as

$$|j\rangle \equiv \hat{a}_j^\dagger |\mathbf{0}\rangle = |0_1, 0_2, \dots, 1_j, \dots, 0_M\rangle, \quad (2)$$

such that the $M \times M$ matrix representation of $\hat{\mathcal{F}}^m$, in the single-particle subspace, is defined as

$$[U_S(mT)]_{ij} \equiv U_{ij}(mT) \equiv \langle i | \hat{\mathcal{F}}^m | j \rangle. \quad (3)$$

The evolution of the bosonic operators can be expressed in the Heisenberg picture as [60]

$$\hat{a}_i^\dagger(mT) = \sum_{j=1}^M U_{i,j}(mT) \hat{a}_j^\dagger. \quad (4)$$

The typical evolution of the operators is illustrated in Fig. 1, where we can interpret the stroboscopic evolution as a photonic quantum circuit with depth mT .

A. Photonic dynamics and permanents

The crucial aspect is that the complexity of the boson sampling problem grows with the number of bosons N in a photonic circuit with M modes. Due to the statistics of the photons, the dimension of the Hilbert space is given by [61]

$${}^{M+N-1}C_N = \frac{(M+N-1)!}{N!(M-1)!}, \quad (5)$$

which corresponds to the number of N -combinations of a set of $M+N-1$ elements [62]. The number of configurations quickly increases with the number of photons. For example, with $N=3$ photons distributed among $M=12$ modes there are ${}^{12}C_3 = 364$ configurations.

The evolution of the quantum state defined in Eq. (1) after m periods of the drive is given by

$$\begin{aligned} |\Psi(mT)\rangle &= \prod_{i=1}^M \frac{[\hat{a}_i^\dagger(mT)]^{n_i^{(I)}}}{[n_i^{(I)}!]^{1/2}} |\mathbf{0}\rangle \\ &= \sum_F \gamma_F(mT) |n_1^{(F)}, n_2^{(F)}, \dots, n_M^{(F)}\rangle, \end{aligned} \quad (6)$$

where F denotes all the possible configurations of N bosonic particles in M modes, while $n_j^{(F)}$ is the population of the j th mode for a given configuration F such that $N = \sum_j n_j^{(F)}$. The probability amplitude $\gamma_F(mT)$ in Eq. (6) also defines the matrix elements of the evolution operator in the N -particle subspace [41, 60]

$$\begin{aligned} \gamma_F(mT) &= \langle n_1^{(I)}, n_2^{(I)}, \dots, n_M^{(I)} | \hat{U}(mT) | n_1^{(F)}, n_2^{(F)}, \dots, n_M^{(F)} \rangle \\ &= \frac{\text{Per}[U^{(F,I)}(mT)]}{\sqrt{n_1^{(F)}! n_2^{(F)}! \dots n_M^{(F)}!}}. \end{aligned} \quad (7)$$

This is given in terms of the permanent of an $N \times N$ submatrix $U^{(F,I)}(mT)$ of $U_S(mT)$. The submatrix $U^{(F,I)}(mT)$ depends on the initial configuration I and the specific configuration F measured at the end of the experiment. More specifically, $U^{(F,I)}(mT)$ is obtained by keeping $n_j^{(F)}$ copies of the j th column and $n_i^{(I)}$ copies of the i th rows. Due to the simplification of the initial configuration I , we only need to choose one copy of a given row of $U_S(mT)$. The corresponding probability of obtaining the configuration F is

$$P_F(mT) = |\gamma_F(mT)|^2 = \frac{|\text{Per}[U^{(F,I)}(mT)]|^2}{n_1^{(F)}! n_2^{(F)}! \dots n_M^{(F)}!}. \quad (8)$$

It is now illustrative to consider the dynamics of the local mean number of photons in mode l , given by

$$\begin{aligned} \langle \hat{n}_l(mT) \rangle &= \langle \Psi(mT) | \hat{a}_l^\dagger \hat{a}_l | \Psi(mT) \rangle \\ &= \sum_F n_l^{(F)} P_F(mT). \end{aligned} \quad (9)$$

We see that measurements with single-photon detectors samples the probability distribution $P_F(mT)$, and thus samples the permanent of the quantum device [42]. The important point of boson sampling is that the problem of calculating the permanent is extremely hard, and in some cases impossible for a classical digital computer [41]. As we will discuss in the following sections, the dynamics in a system that exhibits QSOC is encoded in $U_S(mT)$ and is related to the complexity of the sampling problem.

B. Relation to the Haar measure

In RMT the unitary group together with the Haar measure is referred to as the Circular Unitary ensemble (CUE) [30–32]. In the original paper by Aaronson and Arkhipov [41], a crucial technical aspect of the theory of boson sampling is that the unitary considered in the complexity proof is an $M \times M$ unitary matrix generating the evolution of the modes in Eq. (4) that is chosen randomly according to the Haar measure. This ensures that the distribution of elements of an $N \times N$ submatrix $U^{(F,I)}$ is close in variation distance to i.i.d. complex Gaussian random variables [41].

In the theory of QSOC, it is well known that there is an intimate relation between the properties of chaotic systems and

ensembles of random matrices [9, 31]. Another way to formulate this relation is by analyzing the matrix $U_S(mT)$, which contains information about QSOC at the single-particle level. The fact that we are dealing with photons implies that the output of the sampling experiment is given by a permanent of a submatrix, $U^{(F, D)}(mT)$ of $U_S(mT)$, and not a determinant as is the case of fermions.

Hence, it is reasonable to expect that when the system exhibits QSOC at the single particle level the complexity of the sampling problem should be similar to the case of a matrix chosen from the Haar measure. We are motivated by a recent work that has explored the relation between the problem of sampling bit-strings [63] and the evolution under a unitary of a chaotic system that exhibits circular orthogonal ensemble (COE) level statistics [64]. In the next sections, we will provide a series of intuitive arguments to illustrate how QSOC in our Floquet system may allow for the complexity required to perform boson sampling.

III. QSOC IN PHOTONIC FLOQUET SYSTEMS

In this section we discuss several QSOC that are of interest in the context of our photonic system and we analyze their dynamical consequences for boson sampling. We consider an ensemble of unitary operators, $\mathcal{E}_U \equiv \{\hat{U}_w(T)\}$, indexed by w . In order to investigate QSOC, we examine the properties of the quasienergies, $\{\xi_\alpha^w\}$, and single-particle Floquet states, $\{|\alpha^w\rangle\}$, of the Floquet operator, $\hat{U}_w(T)$, defined from the eigenvalue problem $\hat{U}_w(T)|\alpha^w\rangle = \exp(-i\xi_\alpha^w T/\hbar)|\alpha^w\rangle$, where $-\hbar\pi/T < \xi_\alpha^w < \hbar\pi/T$ [65]. We will compare the spectral statistics of the Floquet operator with ensembles of random matrices in RMT.

A. Quasienergy level statistics

A standard quantity to distinguish ensembles of random matrices is the probability distribution, $P(r)$, of consecutive level spacing ratios [66, 67]

$$r_\alpha^w = \frac{\min(s_\alpha^w, s_{\alpha-1}^w)}{\max(s_\alpha^w, s_{\alpha-1}^w)}, \quad (10)$$

where $s_\alpha^w = \xi_{\alpha+1}^w - \xi_\alpha^w \geq 0$ for adjacent quasienergies ξ_α^w , ordered by increasing energy. We denote r as the level spacing ratio averaged over the ensemble. Eq. (10) has been used successfully to investigate quantum signatures of single- and multi-particle chaos [9, 31], eigenstate thermalization hypothesis [68–70], and manybody localization[71–73]. To compare our system to ensembles of random matrices we compute the spectral average of Eq. (10), given by

$$\langle r \rangle = \frac{1}{|\mathcal{E}_U|} \sum_w \frac{1}{M-2} \sum_\alpha r_\alpha^w, \quad (11)$$

where we have averaged over the ensemble. When calculated from the Wigner surmise in RMT $\langle r \rangle_{\text{Poisson}} \approx 0.38629$ (regular regime) and $\langle r \rangle_{\text{GOE}} \approx 0.53590$ (chaotic regime) [67]. Hence,

Eq. (11) gives an indication when the unitary ensemble has chaotic dynamics.

Even though the probability distribution $P(r)$ is a standard probe used in systems that exhibit QSOC, it only captures local spectral correlations. It misses important long-range spectral correlations [13, 14]. Therefore, it is also useful to look at other quantities associated to the ensemble \mathcal{E}_U in order to probe QSOC. From now on, to simplify the notation, we will neglect the index w denoting a given unitary in the ensemble and present ensemble averaged quantities.

B. Spectral form factors

In the theory of QSOC [9], one is often interested in the correlations between quasienergy levels. This is obtained by the spectral form factors (SFF), which are intimately related to scrambling [22–25] and to other QSOC [9]. The infinite temperature $2N$ -point SFF is given by

$$\mathcal{R}_{2N}(mT) = \sum_{\zeta, \eta} e^{-i(\sum_{\alpha \in \zeta} \xi_\alpha - \sum_{\eta \in \eta} \xi_\eta) mT/\hbar}, \quad (12)$$

where $\zeta = (\zeta_1, \zeta_2, \dots, \zeta_N)$ and $\eta = (\eta_1, \eta_2, \dots, \eta_N)$. Specifically, we will be interested in the two- and four-point SFF

$$\mathcal{R}_2(mT) = \sum_{\alpha, \beta} e^{-i(\xi_\alpha - \xi_\beta) mT/\hbar}, \quad (13)$$

$$\mathcal{R}_4(mT) = \sum_{\alpha, \lambda, \beta, \rho} e^{-i(\xi_\alpha + \xi_\lambda - \xi_\beta - \xi_\rho) mT/\hbar}. \quad (14)$$

The SFF exhibits universal features found in chaotic systems, such as a dip, ramp, and plateau, which will be determined by the symmetries of the Floquet operator. These features are governed by correlations in the quasienergy levels with gaps $\Delta_{\alpha\beta} \equiv \xi_\alpha - \xi_\beta = \sum_{\lambda=\beta}^{\alpha-1} s_\lambda$, that define characteristic time scales $\tau_{\alpha\beta} = \hbar/\Delta_{\alpha\beta}$ in terms of the nearest-neighbor level spacings s_λ . Hence, as time increases, the SFF probes quasienergy correlations that are closer and closer together, until it is dominated by the smallest (largest) energy (time) scale. Therefore, to investigate the manifestations of universal features found in chaotic systems, it is also important to study the time evolution of the spectral correlations found in the SFF.

An important time scale is the Heisenberg time, τ_H , associated to the energy gap $\Delta_{\alpha, \alpha+1} = s_\alpha$ between adjacent quasienergy levels. It is the smallest energy scale (largest time scale), and hence it is dominated by level repulsion in chaotic systems. It can be estimated as $\tau_H = 2\pi\hbar/\langle s \rangle$ [9], where $\langle s \rangle$ is the ensemble averaged level spacing. τ_H is associated with the timescale in finite systems that the discrete energy spectrum can be resolved, and is proportional to the dimension of the Hilbert space, $\tau_H \propto M$. The Heisenberg time is captured in the SFF, where it determines the onset of the plateau where the SFF approaches its asymptotic value.

In RMT the two-point SFF for the GOE is characterized by

the Heisenberg time, and is given by [9, 74]

$$\begin{aligned} \mathcal{R}_2^{\text{GOE}}(mT) &= M^2 r(mT)^2 \\ &+ M \begin{cases} \frac{mT}{\tau_H} - \frac{mT}{\tau_H} \log\left(1 + 2\frac{mT}{\tau_H}\right) & \text{for } 0 < mT \leq \tau_H, \\ 2 - \frac{mT}{\tau_H} \log\left(\frac{2mT/\tau_H + 1}{2mT/\tau_H - 1}\right) & \text{for } mT > \tau_H, \end{cases} \end{aligned} \quad (15)$$

where $r(mT) = \tau_H \mathcal{J}_1(4MmT/\tau_H)/(2MmT)$, and $\mathcal{J}_1(z)$ is the Bessel function of the first kind [75]. At the Heisenberg time, τ_H , the two-point SFF for the GOE approaches the asymptotic value $\mathcal{R}_2^{\text{GOE}}(t \geq \tau_H) = M$.

C. Level repulsion and localization properties of Floquet states

Whether the system is localized or in the quantum chaotic regime will have profound consequences for the boson sampling problem because it will determine the complexity of the multi-particle interference. Let us first investigate the effect of localization and delocalization on the matrix elements of the Floquet operator in the single-particle basis, under the assumption its spectral statistics is that of RMT.

The Floquet operator can be written in the basis of the single-particle Floquet states as $\hat{\mathcal{F}} = \sum_{\alpha} |\alpha\rangle\langle\alpha| e^{-i\xi_{\alpha} T/\hbar}$. Hence, the matrix elements in the single-particle position basis [see Eq. (2)] can be written as

$$U_{i,j}(mT) = \langle i|U(\hat{m}T)|j\rangle = \sum_{\alpha} e^{-i\xi_{\alpha} mT/\hbar} c_{i,\alpha} c_{j,\alpha}^*, \quad (16)$$

where $c_{i,\alpha} = \langle i|\alpha\rangle$.

When a Floquet state, $|\alpha\rangle$, is localized in real space it follows that $|c_{i,\alpha}|^2 \approx \exp(-|i - l_{\alpha}|/\Lambda_{\alpha})$, where Λ_{α} is the localization length, and l_{α} is the center of mass of the wavepacket. That is, most of the contribution to the dynamics is from the diagonal matrix elements of $U_{i,j}(mT)$ within a band $|i - j| < \text{Max}(\Lambda_{\alpha})$, which is determined by the longest localization length scale. We refer the interested reader to Ref. [76] for more information. In terms of the spectrum, localized Floquet states are related to clustering of levels with very small quasienergy gaps [9], and the statistics of the gaps follows a Poissonian distribution because the levels are uncorrelated. Hence, when a photon remains localized in space, it cannot interfere with other photons in remote regions at a distance greater than Λ_{α} , and there is not enough operator spreading (see next section) to perform boson sampling.

Next, let us briefly discuss the onset of thermalization in our Floquet bosonic system and how it affects localization properties of Floquet states. As the Floquet operator is unitary, it can be written in terms of an effective Hamiltonian \hat{H}_{eff} as $\hat{\mathcal{F}} = e^{-i\hat{H}_{\text{eff}}T/\hbar}$. To talk about thermalization, it is important to identify the conserved quantities of our Floquet system. Previous works define these conserved quantities for fermionic quadratic Hamiltonians [77]. Here we extend the theory for bosons by defining the operator $b_{\alpha}^{\dagger} \equiv \sum_r c_{r,\alpha}^* \hat{a}_r^{\dagger}$ that creates bosonic particles in the α quasienergy state, i.e., $|\alpha\rangle \equiv b_{\alpha}^{\dagger}|\mathbf{0}\rangle$. As our system is quadratic in the bosonic operators, the effective Hamiltonian is also quadratic and can be written as a

system of free bosons $\hat{H}_{\text{eff}} = \sum_{\alpha} \xi_{\alpha} b_{\alpha}^{\dagger} b_{\alpha}$. This naturally defines a set $\{\hat{\mathcal{I}}_{\alpha}\}$ of conserved quantities $\hat{\mathcal{I}}_{\alpha} = b_{\alpha}^{\dagger} b_{\alpha}$.

In the long-time limit, the system is known to reach a steady state known as the Floquet generalized Gibbs ensemble [77], described by a density matrix

$$\hat{\rho}_{\text{GGE}} = \frac{1}{Z} e^{-\sum_{\mu} \Gamma_{\mu} b_{\mu}^{\dagger} b_{\mu}} = \frac{1}{Z} \sum_{\alpha} |\alpha\rangle\langle\alpha| e^{-\Gamma_{\alpha} \xi_{\alpha}}, \quad (17)$$

where $\Gamma_{\alpha} = 1/k_B T_{\alpha}$ and T_{α} are effective temperatures determined by the conserved quantities, while Z is a normalization constant. Further, we can deduce that $|c_{i,\alpha}|^2 \approx e^{-\Gamma_{\alpha} \xi_{\alpha}}/Z$ (see Appendix A) [77]. Thus, the steady state is Gaussian and determined by different effective temperatures. In certain parameter regimes, the system can heat up to infinite temperatures [78–80]. In this case, one obtains fully delocalized Floquet states with $|c_{i,\alpha}|^2 \approx 1/M$ and the quasienergies exhibit strong level repulsion following COE statistics, while $\{\xi_{\alpha}\}$ behave like incommensurable phases [78]. Intuitively, we expect thermalized systems to be more useful for boson sampling as the photons can explore more modes and interfere, which increases the complexity of the problem.

IV. OUT-OF-TIME-ORDER CORRELATORS (OTOC) AND BOSON SAMPLING

In this section we introduce one of our key results. One way to capture long-range spectral correlations is to investigate the dynamics of out-of-time-order correlators (OTOCs) [21, 81]. We will define a $2N$ -point OTOC and show that it is equal to performing N -particle boson sampling and calculating the permanent (see Eq. (8)). Hence the properties of the OTOC gives information about the complexity of the Floquet operator and how hard the boson sampling task is.

The simple form of the evolution of the modes (see Eq. (4)) motivates us to investigate the following two-point OTOC,

$$C_{i,j}^{(2)}(mT) = \langle \mathbf{0} | [\hat{a}_i^{\dagger}(mT), \hat{a}_j]^{\dagger} [\hat{a}_i^{\dagger}(mT), \hat{a}_j] | \mathbf{0} \rangle. \quad (18)$$

Using Eq. (4) this can be simply evaluated, giving

$$\begin{aligned} C_{i,j}^{(2)}(mT) &= U_{ij}^*(mT) U_{ij}(mT) \\ &= \sum_{\alpha,\beta} c_{i,\alpha} c_{j,\alpha}^* c_{i,\beta} c_{j,\beta} e^{-i(\xi_{\alpha} - \xi_{\beta})mT/\hbar} \\ &= P_F(mT). \end{aligned} \quad (19)$$

We see that the two-point OTOC is calculated from the permanent as in Eq. (7), and is obtained from a single-particle ($N = 1$) boson sampling experiment.

As we previously discussed, when there is strong level repulsion with RMT spectral statistics, one has $|c_{i,\alpha}|^2 \approx e^{-\Gamma_{\alpha} \xi_{\alpha}}/Z$ [77]. If the systems heats up to infinite temperature, the Floquet states become delocalized. In this situation, using Eq. (16), the two-point OTOC is approximately

$$C_{i,j}^{(2)}(mT) \approx \frac{\mathcal{R}_2(mT)}{M^2}. \quad (20)$$

This naturally establishes the relation between our photonic OTOC and the two-point SFF, $\mathcal{R}_2(mT)$, given by Eq. (13).

Next, let us discuss the four-point OTOC, given by

$$\hat{C}_{i,j,r,s}^{(4)}(mT) = \langle \mathbf{0} | \hat{C}_{i,j,r,s}^\dagger(mT) \hat{C}_{i,j,r,s}(mT) | \mathbf{0} \rangle, \quad (21)$$

where $\hat{C}_{i,j,r,s}(mT) = [\hat{a}_i^\dagger(mT) \hat{a}_j^\dagger(mT), \hat{a}_r \hat{a}_s]$. To evaluate this, it is enough to look at the expression

$$\begin{aligned} \hat{C}_{i,j,r,s}(mT) | \mathbf{0} \rangle &= \sum_{o,p} U_{i,o}(mT) U_{j,p}(mT) \hat{a}_r \hat{a}_s \hat{a}_o^\dagger \hat{a}_p^\dagger | \mathbf{0} \rangle \\ &= [U_{i,r}(mT) U_{j,s}(mT) + U_{i,s}(mT) U_{j,r}(mT)] | \mathbf{0} \rangle. \end{aligned} \quad (22)$$

From this we can directly obtain the 4-point OTOC

$$\hat{C}_{i,j,r,s}^{(4)}(mT) = P_F(mT) = \left| \text{Per} \left[U^{(F,I)}(mT) \right] \right|^2, \quad (23)$$

where $\text{Per} \left[U^{(F,I)}(mT) \right]$ denotes the permanent of a submatrix

$$U^{(F,I)} = \begin{bmatrix} U_{i,r}(mT) & U_{i,s}(mT) \\ U_{j,r}(mT) & U_{j,s}(mT) \end{bmatrix}, \quad (24)$$

of $U_S(mT)$. In Eq. (8), we used $P_F(mT) = |\gamma_F(mT)|^2$ that is determined by the probability amplitude

$$\begin{aligned} \gamma_F(mT) &= \langle \mathbf{0} | \hat{a}_s \hat{a}_r | \Psi(mT) \rangle \\ &= U_{i,r}(mT) U_{j,s}(mT) + U_{i,s}(mT) U_{j,r}(mT), \end{aligned} \quad (25)$$

of having the configuration $\hat{a}_r^\dagger \hat{a}_s^\dagger | \mathbf{0} \rangle$ provided that we initially prepare a two-photon state $|\Psi(0)\rangle = \hat{a}_i^\dagger \hat{a}_j^\dagger | \mathbf{0} \rangle$ and let the system evolve m periods. This establishes a relation between $\hat{C}_{i,j,r,s}^{(4)}(mT)$, operator spreading, and two-particle boson sampling ($N = 2$). In a similar fashion to the single-particle case, when the system exhibits level repulsion, the correlator $\hat{C}_{i,j,r,s}^{(4)}(mT)$ can be written in terms of the four-point SFF, $\mathcal{R}_4(mT)$, given by Eq. (14).

The examples presented so far for few particles gives insight on how to generalize the photonic OTOC for multiple particles. In a system with N input photons, the general OTOC corresponds to measuring a $2N$ -point correlator $\hat{C}_{I,F}^{(2N)}(mT) = \langle \mathbf{0} | \hat{C}_{I,F}^\dagger(mT) \hat{C}_{I,F}(mT) | \mathbf{0} \rangle$, where we define the operator $\hat{C}_{I,F}(mT) = [\prod_{i \in I} [\hat{a}_i^\dagger(mT)]^{n_i^{(I)}}, \prod_{j \in F} [\hat{a}_j]^{n_j^{(F)}}]$, and I and F are, respectively, the initial and final configurations of N photons in M modes. Consequently, the $2N$ -point OTOC is given by

$$\hat{C}_{I,F}^{(2N)}(mT) = P_F(mT) = \frac{\left| \text{Per} \left[U^{(F,I)}(mT) \right] \right|^2}{n_1^{(F)}! n_2^{(F)}! \cdots n_M^{(F)}!}. \quad (26)$$

In the chaotic regime the $2N$ -point photonic OTOC is proportional to the $2N$ -point SFF, $\mathcal{R}_{2N}(mT)$, given by Eq. (12).

The important message we want to convey is that measuring the probability amplitude, $P_F(mT)$, is equivalent to measuring a photonic OTOC. We will show, with an example, that when the system exhibits QSOC that boson sampling should

be hard [see Section VIII D]. This is linked with the OTOC and scrambling [21] in the chaotic regime, where in a system with QSOC operators spread across all modes, but instead do not in the regular regime. Thus, whether the boson sampling task is hard depends on the periodic photonic chips capability to scramble information and become delocalized [see Fig. 1].

In the next section we will show how the two- and four-point SFF will naturally appear in the dynamics of expectation values and how they determine long-time properties such as equilibration due to level repulsion.

V. FLOQUET THEORY AND QUANTUM DYNAMICS OF LOCAL OBSERVABLES

In this section we discuss another important result of our work. Here we show the intimate relation between QSOC and the dynamics of the system. In particular, we will explore how single-particle signatures of chaos influence the dynamics of observables in a multi-particle scenario. We will show that when the single-particle unitary matrix $U_S(mT)$ [with elements $U_{i,j}(mT)$] exhibits spectral properties related to RMT, the single-particle dynamics reaches the periodic steady state $\hat{\rho}_{\text{GGE}}$, given by Eq. (17), that is diagonal in the basis of Floquet states. This is solely determined by the strong repulsion of quasienergy levels that is characteristic of chaotic systems. For simplicity, we focus on the single- and two-particle case, but the results and conclusions presented here are valid for any number of particles.

A. Single-particle dynamics

As a first step, it is useful to discuss the effect of QSOC on the dynamics of local observables at the single-particle level. In particular, we will explore the consequences of quasienergy level repulsion with GOE statistics [9, 31]. In Section VII of our paper, we will show an example of a unitary that exhibits spectral statistics consistent with the Gaussian Orthogonal Ensemble (GOE) [31].

Let us investigate what happens with the dynamics of a single particle initialized in the state $|\psi(0)\rangle = \hat{a}_i^\dagger | \mathbf{0} \rangle$ in the regular and chaotic regimes. After m periods of the circuit, the evolution of the particle is given by

$$|\psi(mT)\rangle = \sum_r U_{i,r}(mT) \hat{a}_r^\dagger | \mathbf{0} \rangle = \sum_\alpha e^{-i\xi_\alpha mT/\hbar} c_{i,\alpha} b_\alpha^\dagger | \mathbf{0} \rangle. \quad (27)$$

To investigate long-time properties of the system due to level repulsion, such as equilibration [82], it is useful to define the time average of observables. For example, the time-averaged number of photons at a given site l over a total number \mathcal{M} of periods of the drive is given by

$$\begin{aligned} \bar{n}_l &= \frac{1}{\mathcal{M}} \sum_{m=0}^{\mathcal{M}-1} \langle \hat{n}_l(mT) \rangle = \frac{1}{\mathcal{M}} \sum_{m=0}^{\mathcal{M}-1} P_F(mT) \\ &= \frac{1}{\mathcal{M}} \sum_{m=0}^{\mathcal{M}-1} \sum_{\alpha,\beta} e^{-i(\xi_\alpha - \xi_\beta)mT/\hbar} c_{i,\alpha} c_{i,\beta}^* c_{l,\alpha} c_{l,\beta}^*, \end{aligned} \quad (28)$$

where we have used Eq. (9) that relates \hat{n}_l and $P_F(mT)$. It is worth noticing that the expression for \bar{n}_l resembles the two-point SFF $\mathcal{R}_2(mT)$ in Eq. (13). The dynamics of observables is determined by the quasienergy gaps and the spectral correlations that are encoded in the SFF.

For example, when the system is in the regular regime, the quasienergy gaps become uncorrelated [8, 9] and usually they are also small thus defining a set of long time scales $\tau_{\alpha,\beta} = \hbar/\Delta_{\alpha,\beta}$ discussed above. Further, when the system is close to a degeneracy point or if it exhibit clustering of levels, then it is not able to equilibrate as the average in Eq. (28) contains off-diagonal elements $\langle \beta | \hat{n}_l | \alpha \rangle$ with $\alpha \neq \beta$. On the other hand, when the system exhibits QSOC, the system not only equilibrates but it also thermalizes in the sense of ETH at time scales $\mathcal{M}T \gg \text{Max}(\tau_{\alpha,\beta})$ [82] with

$$\bar{n}_l = \sum_{\alpha} |c_{l,\alpha}|^2 |c_{l,\alpha}|^2, \quad (29)$$

where we have used the fact that $\langle \alpha | \hat{n}_l | \alpha \rangle = |c_{l,\alpha}|^2$. This expression can be obtained by assuming that the eigenphases are incommensurable and thus the only term that contribute after the time average is given by the diagonal matrix elements of the observable in the single-particle Floquet basis. In Appendix A we provide a formal derivation of this time average. Further, we can deduce that when the system thermalizes [77, 82], $\bar{n}_l = \text{tr}(\hat{\rho}_{\text{GGE}} \hat{n}_l)$ (see Appendix A), where $\hat{\rho}_{\text{GGE}}$ is the Floquet generalized Gibbs states in Eq. (17). At infinite temperature, the Floquet states are fully delocalized in space and $|c_{l,\alpha}|^2 = 1/M$. Thus, the average local number of photons scales as $\bar{n}_l \sim 1/M$. As a consequence of Eqs. (28) and (29), we obtain the time averaged probability scaling as $\bar{P}_F = 1/\mathcal{M} \sum_{m=1}^{\mathcal{M}} P_F(mT) \sim 1/M$.

B. Two-particle dynamics

Now let us consider the two-particle case, which will give us insight on the interplay between single-particle chaos and the bosonic character of the particles. Similarly to the single particle case, we investigate the evolution of an initial two particle state $|\Psi(0)\rangle = \hat{a}_i^\dagger \hat{a}_j^\dagger |0\rangle$. After m periods, the state evolves to

$$\begin{aligned} |\Psi(mT)\rangle &= \hat{a}_i^\dagger(mT) \hat{a}_j^\dagger(mT) |0\rangle \\ &= \sum_{r,s=1}^M U_{i,r}(mT) U_{j,s}(mT) \hat{a}_r^\dagger \hat{a}_s^\dagger |0\rangle. \end{aligned} \quad (30)$$

Next, let us calculate how the single-particle QSOC influence the long-time behavior of

$$P_F(mT) = |U_{i,r}(mT) U_{j,s}(mT) + U_{i,s}(mT) U_{j,r}(mT)|^2, \quad (31)$$

which is obtained from the probability amplitude in Eq. (25). To see how the level repulsion affects the dynamics, it is convenient to use Eq. (16) to write the probability in terms of

Floquet states

$$\begin{aligned} P_F(mT) &= \sum_{\alpha,\lambda,\beta,\rho} e^{-i(\xi_\alpha + \xi_\lambda - \xi_\beta - \xi_\rho)mT/\hbar} \left(W_{i,j,r,s}^{\alpha,\lambda,\beta,\rho} + W_{i,j,s,r}^{\alpha,\lambda,\beta,\rho} \right) \\ &+ 2\text{Re} \left[\sum_{\alpha,\lambda,\beta,\rho} e^{-i(\xi_\alpha + \xi_\lambda - \xi_\beta - \xi_\rho)mT/\hbar} S_{i,j,r,s}^{\alpha,\lambda,\beta,\rho} \right], \end{aligned} \quad (32)$$

where we have defined

$$\begin{aligned} W_{i,j,r,s}^{\alpha,\lambda,\beta,\rho} &= c_{i,\alpha} c_{r,\alpha}^* c_{j,\lambda} c_{s,\lambda}^* c_{i,\beta} c_{r,\beta} c_{j,\rho}^* c_{s,\rho} \\ S_{i,j,r,s}^{\alpha,\lambda,\beta,\rho} &= c_{i,\alpha} c_{r,\alpha}^* c_{j,\lambda} c_{s,\lambda}^* c_{i,\beta}^* c_{s,\beta} c_{j,\rho}^* c_{r,\rho}. \end{aligned} \quad (33)$$

As we are exploring here the dynamics of two particles, it is expected that the dynamics strongly depends on correlations between four single-particle quasienergy levels, which is captured the spectral form factor $\mathcal{R}_4(mT)$ [see Eq. (14)].

In Appendix A we describe in detail how to perform the time average of this quantity in the chaotic regime to obtain

$$\begin{aligned} \bar{P}_F &= \sum_{\alpha,\lambda} \left(W_{i,j,r,s}^{\alpha,\lambda,\alpha,\lambda} + W_{i,j,r,s}^{\alpha,\lambda,\lambda,\alpha} + W_{i,j,s,r}^{\alpha,\lambda,\alpha,\lambda} + W_{i,j,s,r}^{\alpha,\lambda,\lambda,\alpha} \right) \\ &+ 2\text{Re} \left[\sum_{\alpha,\lambda} \left(S_{i,j,r,s}^{\alpha,\lambda,\alpha,\lambda} + S_{i,j,r,s}^{\alpha,\lambda,\lambda,\alpha} \right) \right]. \end{aligned} \quad (34)$$

The most important information we want to extract from this time average is the scaling of the probability $\bar{P}_F \sim 1/M^2$ for each configuration because $W_{i,j,r,s}^{\alpha,\lambda,\lambda,\alpha} \approx S_{i,j,r,s}^{\alpha,\lambda,\lambda,\alpha} \approx 1/M^4$ (assuming that the single-particle system thermalizes at infinite temperature). This is the approximate scaling that the probability \bar{P}_F reaches when the system equilibrates.

We can also write the expression for the state in terms of Floquet states

$$|\Psi(mT)\rangle = \sum_{\alpha,\lambda} e^{-i(\xi_\alpha + \xi_\lambda)mT/\hbar} c_{i,\alpha} c_{j,\lambda} b_\alpha^\dagger b_\lambda^\dagger |0\rangle. \quad (35)$$

As expected, the evolution of two photons is determined by a two-particle quasienergy $E_{\alpha,\lambda} = \epsilon_\alpha + \epsilon_\lambda$ and is given by a quantum superposition of two particles occupying the different available Floquet states. This equation contains valuable information as the overlaps $c_{i,\alpha} = \langle i | \alpha \rangle$ and $c_{j,\lambda} = \langle j | \lambda \rangle$ contain information about localization properties of the Floquet states, the two particle quasienergies carry information about spectral properties of the system, and the operators b_α^\dagger allows us to keep track of the bosonic character of the photons. We can show that

$$\bar{n}_l = \frac{1}{\mathcal{M}} \sum_{m=0}^{\mathcal{M}} \sum_{\alpha,\lambda,\beta,\rho} e^{-i(\xi_\alpha + \xi_\lambda - \xi_\beta - \xi_\rho)mT/\hbar} O_{i,j}^{\alpha,\lambda,\beta,\rho} \langle 0 | b_\beta b_\rho \hat{n}_l b_\alpha^\dagger b_\lambda^\dagger | 0 \rangle, \quad (36)$$

where $O_{i,j}^{\alpha,\lambda,\beta,\rho} = c_{i,\alpha} c_{j,\lambda} c_{i,\beta}^* c_{j,\rho}^*$.

In contrast to the single-particle case, here we need to be cautious and take into account the bosonic character of the

particles. For this reason, let us investigate in detail the vacuum expectation value

$$\begin{aligned} \langle 0|b_\beta b_\rho \hat{n}_l b_\alpha^\dagger b_\lambda^\dagger|0\rangle &= \sum_{\sigma,\eta} c_{l,\sigma} c_{l,\eta}^* \langle 0|b_\beta b_\rho \hat{b}_\sigma^\dagger \hat{b}_\eta b_\alpha^\dagger b_\lambda^\dagger|0\rangle \\ &= c_{l,\rho} c_{l,\lambda}^* \delta_{\alpha,\beta} + c_{l,\rho} c_{l,\alpha}^* \delta_{\beta,\lambda} \\ &\quad + c_{l,\beta} c_{l,\lambda}^* \delta_{\alpha,\rho} + c_{l,\beta} c_{l,\alpha}^* \delta_{\rho,\lambda}, \end{aligned} \quad (37)$$

where we have used that $\hat{n}_l = \hat{a}_l^\dagger \hat{a}_l = \sum_{\sigma,\eta} c_{l,\sigma} c_{l,\eta}^* \hat{b}_\sigma^\dagger \hat{b}_\eta$ and the identity

$$\begin{aligned} \langle 0|b_\beta b_\rho \hat{b}_\sigma^\dagger \hat{b}_\eta b_\alpha^\dagger b_\lambda^\dagger|0\rangle &= \delta_{\rho,\sigma} (\delta_{\eta,\lambda} \delta_{\alpha,\beta} + \delta_{\eta,\alpha} \delta_{\lambda,\beta}) \\ &\quad + \delta_{\beta,\sigma} (\delta_{\eta,\lambda} \delta_{\alpha,\rho} + \delta_{\eta,\alpha} \delta_{\lambda,\rho}). \end{aligned} \quad (38)$$

In the chaotic regime, there are no degeneracies in the quasienergy spectrum and by using the relations discussed above we can explicitly derive the time average in Eq. (36) as

$$\begin{aligned} \bar{n}_l &\approx \sum_{\alpha,\lambda} O_{i,j}^{\alpha,\lambda,\alpha,\lambda} |c_{l,\lambda}|^2 + O_{i,j}^{\alpha,\lambda,\lambda,\alpha} |c_{l,\alpha}|^2 \\ &\quad + \sum_{\alpha,\lambda} O_{i,j}^{\alpha,\lambda,\lambda,\alpha} |c_{l,\lambda}|^2 + O_{i,j}^{\alpha,\lambda,\alpha,\lambda} |c_{l,\alpha}|^2. \end{aligned} \quad (39)$$

Similarly to the single-particle case, the average local number of photons scales as $\bar{n}_l \sim 1/M$ when the system equilibrates.

At this point, it is important to emphasize that at the single-particle level we assume a general system with RMT level statistics. From the theory of generalized thermalization of Floquet systems, this implies that such a system thermalizes at a given temperature determined by conserved quantities as in Ref. [82]. In the multiparticle case, however, the local observables do not thermalize but they equilibrate [82]. In fact, in a recent experiment, local equilibration [83] was observed in an optical simulation of undriven Hamiltonians. The scalings that we have obtained from the time averages give us some intuition of the values of observables after equilibration takes place.

From the results presented in this section, we can see the intimate relation between the calculation of time averages and spectral correlations. We can also see how to generalize this to the N -particle case. In this situation, the dynamics is determined by $2N$ -point level correlations encoded in the spectral form factor $\mathcal{R}_{2N}(mT)$. The level repulsion set the time scales for equilibration [82].

VI. COMPLEXITY OF BOSON SAMPLING AND RELATION TO QSOC

As we mentioned above, in our work our aim is to understand the relation between single-particle chaotic evolution and the inherent complexity of boson sampling. Our results thus far show a relation between QSOC in periodic photonic circuits, such as OTOCs, spectral form factors and equilibration of observables. However, the results presented so far are not enough evidence to show that chaotic systems provide the complexity required for a boson sampling task to be hard. In

fact, although the unitary $U_S(mT)$ exhibits chaotic spectral statistics, it is not guaranteed at all that such a unitary is close to a random matrix drawn from the CUE. Therefore, to discuss the complexity of sampling, we cannot invoke the argument used in the original paper by Aaronson and Arkhipov based on properties of the Haar measure [41].

To have a deeper understanding of the caveats here, we need to look at the arguments presented in the original paper of Aaronson and Arkhipov [41]. To set the basis for the first argument, we remind the reader that in their work, Aaronson and Arkhipov wrote that given a general matrix $A \in C^{N \times N}$, the problem of approximating $\text{Per}(A)$ to within a constant factor is #P complete. In our case, the chaotic dynamics renders a $N \times N$ submatrix $U^{(F,I)}(mT)$ that is obviously complex.

To show that the estimation of the permanent is #P-hard, one requires an additional ingredient based on the assumption that the matrix $U_S(mT)$ is drawn from the CUE. In their work, Aaronson and Arkhipov discuss the motivation of choosing unitaries drawn from the Haar measure to perform boson sampling. The idea is that given a random matrix \hat{U} chosen randomly according to the Haar measure, then any $N \times N$ submatrix $U^{(F,I)}$ of \hat{U} will be close (provided a suitable distance) to a matrix of i.i.d. Gaussians when $N < M^{1/6}$ [41]. Thus, unitaries from the Haar measure naturally provide submatrices that are Gaussian. Further, Gaussian matrices are extremely important because one can invoke the ‘‘Permanent-of-Gaussians Conjecture’’ to show that the Gaussian Permanent Estimation (GPE) problem is #P-hard.

All of this being said, to have some intuition about how complex our dynamics is, we need to investigate statistical properties of the submatrix $U^{(F,I)}(mT)$. Intuitively, this makes sense because the matrix $U_S(mT)$ generates the dynamics of the modes in the Heisenberg picture, and thus it determines the operator spreading. In other words, to achieve the complexity required for boson sampling, we need to let the system evolve for enough time to have enough information scrambling. For example, if the disorder is too strong, the operator spreading shows a logarithmic light cone characteristic of anomalous diffusion [76]. Due to disorder, some modes cannot be reached during the evolution. In a multiparticle scenario, this would limit the photon interference and certain submatrices $U^{(F,I)}(mT)$ will not show Gaussian statistics. A direct consequence of this is that the permanent for those atypical configurations is not hard (see Fig. 1).

In the chaotic regime, the operator scrambling resembles diffusive behavior and photon interference is enhanced. This situation enables more information scrambling, and hence, the matrix $U^{(F,I)}(mT)$ shows Gaussian statistics.

VII. AN EXAMPLE MODEL: A HYBRID OPTICAL FLOQUET CIRCUIT

The results presented so far are general and valid for any unitary operator. Our aim in this section is to provide a concrete example of a system that undergoes a crossover from regular to chaotic behavior.

Next, we will propose a time-periodic photonic system,

where within a period of the drive, T , the evolution is given by a succession of two operators. First one applies a pattern of local phase shift unitaries, given by

$$\hat{U}_1 \equiv \prod_{j=1}^M \exp(-i\tilde{\phi}_j \hat{a}_j^\dagger \hat{a}_j), \quad (40)$$

where \hat{a}_j^\dagger creates a photon in mode j , \hat{a}_j annihilates a photon, $\tilde{\phi}_j$ is the angle of the phase shifter, and M is the total number of modes. Then a unitary is applied that acts like an M -port beam splitter characterized by an angle θ , given by

$$\hat{U}_2 \equiv \exp\left[-i\theta \sum_{j=1}^M (\hat{a}_j^\dagger \hat{a}_{j+1} + \hat{a}_{j+1}^\dagger \hat{a}_j)\right]. \quad (41)$$

Hence, the evolution operator in one period of the drive is given by $\hat{\mathcal{F}} \equiv \hat{U}_2 \hat{U}_1$, where

$$\hat{\mathcal{F}} = \exp\left[-i\theta \sum_{j=1}^M (\hat{a}_j^\dagger \hat{a}_{j+1} + \hat{a}_{j+1}^\dagger \hat{a}_j)\right] \prod_{j=1}^M \exp(-i\tilde{\phi}_j \hat{a}_j^\dagger \hat{a}_j), \quad (42)$$

is the Floquet operator [9, 58].

The unitary given by Eq. (42) is general. We propose that it can be physically realized in silica-on-silicon waveguide circuits consisting of M accessible spatial modes [60, 84], which we schematically depict in Fig. 2. For a period of the drive, the waveguides are separated at the beginning to avoid evanescent coupling and phase-shifters are used to implement \hat{U}_1 . Then, as the photons travel along the chip, the waveguides are quickly brought together, allowing for evanescent coupling [59], which implements \hat{U}_2 . The strength of the evanescent coupling controls the parameter θ .

A. Quantum kicked rotor

To obtain some physical intuition of the dynamics generated by our hybrid quantum circuit, it is useful to consider a time-periodic Hamiltonian $\hat{H}(t) = \hat{H}(t + T)$, whose unitary time evolution in one period is given by Eq. (42). The corresponding Hamiltonian is a kicked rotor, given by

$$\hat{H}(t) = \sum_{j=1}^M \frac{\hbar \tilde{\phi}_j}{T} \hat{a}_j^\dagger \hat{a}_j + \frac{\hbar \theta}{T} \sum_{m=-\infty}^{\infty} \delta(t/T - m) \sum_{j=1}^M (\hat{a}_j^\dagger \hat{a}_{j+1} + \text{h.c.}), \quad (43)$$

where the first term is a spatial modulation of onsite energies, and the second term is a periodic train of delta kicks, with kicking strength $\hbar\theta/T$, that couples nearest-neighbor modes. We define a spatial profile of the onsite angular frequency detunings

$$\tilde{\phi}_j = \phi_j + \delta_j, \quad (44)$$

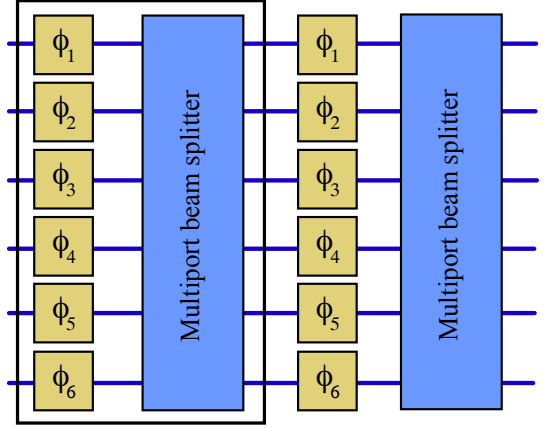
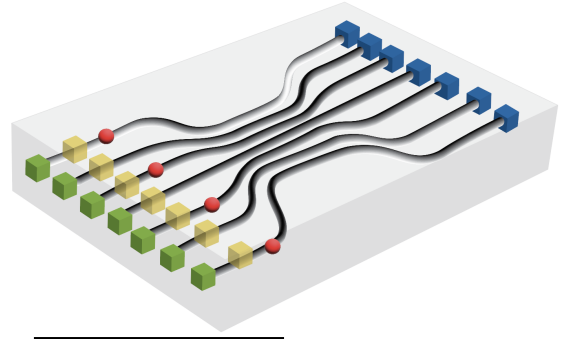


FIG. 2. Schematic of a photonic chip that implements the dynamics of the kicked rotor (see Eq. (43)), for demonstrating boson sampling. The yellow boxes represent the local phase-shifter \hat{U}_1 (see Eq. (41)). The multiport beam splitter is achieved by bringing the waveguides together, which implements the unitary \hat{U}_2 (see Eq. (41)). The black box is one cycle of the drive, whose dynamics is given by the Floquet operator $\hat{\mathcal{F}}$ (see Eq. (42)).

where

$$\phi_j = \frac{4\Phi}{M^2} \left(j - \frac{M}{2}\right)^2, \quad (45)$$

acts as a harmonic trapping potential with strength Φ , and δ_j is a random angle drawn from a uniform distribution in the interval $[-W, W]$.

It is important to emphasize that the Hamiltonian given by Eq. (43) does not contain interactions between the particles, i.e., it is quadratic in the bosonic operators. As the particles are non-interacting, each particle independently evolves under the time evolution operator $\hat{U}(mT)$. However, interesting physics, such as multiparticle interference [44, 45], occurs in the case of multiple bosonic particles due to their statistics [85].

In our photonic implementation, by adding disorder to the phase-shifters, we define an ensemble of unitaries associated to the dynamics generated by the quantum kicked rotor. The effect of a small amount of disorder is to break any remaining symmetries in our system. At the single particle level this allows the system to thermalize, as has been recently reported in the context of undriven systems [82]. If the disorder is too strong, however, the system becomes localized. In the next

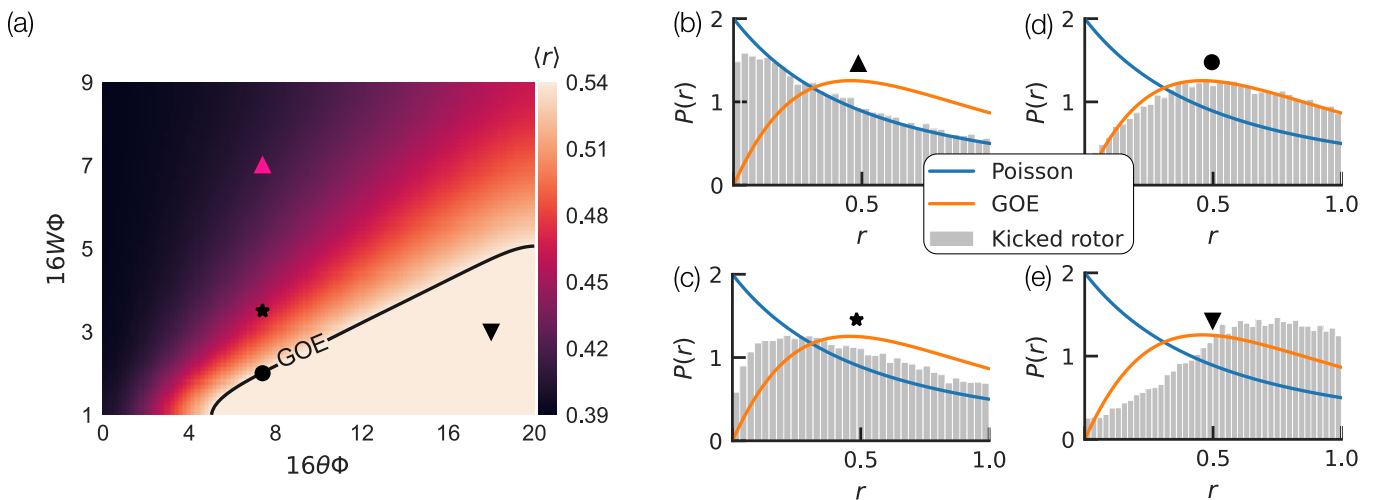


FIG. 3. There is a crossover from Poissonian to Gaussian Orthogonal Ensemble (GOE) statistics in the consecutive level spacing ratio, $\langle r \rangle$. (a) The average $\langle r \rangle$, where θ is the rotation angle of the M -port beam splitter, and Φ is the strength of the harmonic trapping potential. The contour line delineates $\langle r \rangle = 0.53590$ for the GOE. The probability distribution of consecutive level spacing ratios, $P(r)$, is depicted in (b) $W = 7/(16\Phi)$ and $\theta = 7.4/(16\Phi)$ (upward triangle); (c) $W = 3.5/(16\Phi)$ and $\theta = 7.4/(16\Phi)$ (star); (d) $W = 2/(16\Phi)$ and $\theta = 7.4/(16\Phi)$ (circle); (e) $W = 3/(16\Phi)$ and $\theta = 18/(16\Phi)$ (downward triangle). Calculated for $|\mathcal{E}_U| = 100$ disorder realizations, $M = 300$ modes, $\Phi = \pi/4$, and $T = 1$.

section, we will show that both θ as well as W are key parameters describing the transition between regular and chaotic behavior in our system.

B. Classical kicked rotor and chaos

Following the procedure outlined in [86], in the absence of disorder ($W = 0$), one can obtain a semiclassical limit of Eq. (43) in the single-particle subspace. Here the size M of the chain determines the effective Planck constant given by $\hbar_{\text{eff}} = \hbar/M$. In this way, we can derive a semiclassical Hamiltonian for $M \gg 1$ in terms of the dimensionless canonical variables x and k [see Appendix B for its derivation], given by

$$\mathcal{H}_{\text{sc}}(x, k, t) = \frac{4\hbar\Phi}{T} \left(x - \frac{1}{2} \right)^2 + \frac{2\hbar\theta}{T} \sum_{m=-\infty}^{\infty} \delta(t/T - m) \cos(k). \quad (46)$$

The resulting Hamiltonian has a very similar form to the classical kicked rotor, which is a paradigmatic model of chaotic dynamics [50–56]. In Appendix B we show that Eq. (46) exhibits a crossover from regular to chaos [56]. For example, when $\theta = 1/(8\Phi)$ the system is regular with a mixed phase space, while for $\theta = 5/(8\Phi)$ the system is fully chaotic.

The semi-classical limit is obtained in the limit of an infinite chain. However, in experimental platforms one works with a finite number of sites M – usually a few of them – far from the semiclassical limit. A natural question is whether the chaotic dynamics found in the classical kicked rotor are also exhibited in the finite sized quantum kicked rotor. We will show in that the quantum kicked rotor defined in Eq. (43) exhibits a crossover to a regime that exhibits QSOC associated with the classical rotor defined in Eq. (46).

VIII. NUMERICAL RESULTS

The purpose of this section is to show numerical results for our particular example of a photonic Floquet circuit. Numerically, we generate $w = 1, \dots, |\mathcal{E}_U|$ realizations of the Floquet operator Eq. (42) which are uniformly distributed with probability $p_w = 1/|\mathcal{E}_U|$. We show results for the level statistics, spectral form factors and the dynamics of observables. We also show key numerical evidence that the submatrices $U^{(F, D)}(mT)$ of the unitary $U_S(mT)$ show Gaussian statistics. This is an indication that chaotic system exhibit the complexity required for boson sampling tasks to be hard.

A. Quasienergy level statistics

Fig. 3 shows $\langle r \rangle$ [see Eq. (11)] as a function of the M -port beam splitter rotation angle (kicking strength), θ , and onsite disorder strength W . When disorder dominates, the system is localized in real space with a Poisson distribution. For large kicking that dominates over disorder, pseudoconservation of crystal momentum is recovered and the system is instead localized in momentum space. The competition between kicking and disorder promotes quasienergy level repulsion ($P(r) \sim r$ for GOE), giving large regions where the level statistics appears chaotic.

In the regions where $\langle r \rangle \neq \langle r \rangle_{\text{GOE}}$, the probability distribution $P(r)$ deviates from the ones exactly calculated from the Wigner surmise, as shown in Fig. 3. In fact, there is a crossover between regions, as is expected for systems exhibiting single-particle chaos [9]. The quasienergy level statistics gives an indication of where the system is chaotic, and we will confirm this by looking for universal features found in the SFF

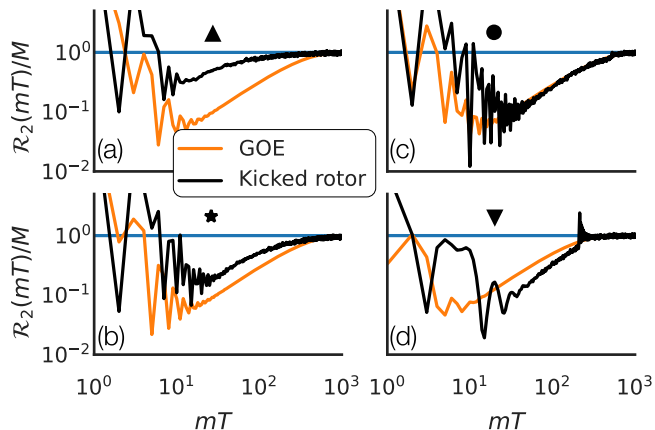


FIG. 4. Stroboscopic dynamics of the two-point spectral form factors, $\mathcal{R}_2(mT)$ [see Eq. (13)], shows the characteristic dip, ramp, and plateau of chaotic systems. When the spectral statistics are (a) Poissonian the SFF is close to the long-time asymptote $\bar{\mathcal{R}}_2 = M$ (blue horizontal line). Instead, in (c)-(d) the SFF more closely resembles that expected in a chaotic system [see Eq. (15)], with a dip, ramp, and plateau. In the crossover regime (b) the kicked rotor exhibits weak QSOC. We set the Heisenberg time as (a) $\tau_H \approx 535T$, (b) $585T$, (c) $605T$, (d) $300T$. The upwards triangle, star, circle, and downwards triangle correspond to the subfigures in Fig. 3. Calculated for $|\mathcal{E}_U| = 1000$ disorder realizations and $M = 300$ modes.

for systems that exhibit QSOC.

B. Spectral form factors

For a general chaotic photonic system with $N \ll M$ the SFF $\mathcal{R}_{2N}(mT)$ [see Eq. (12)] shows a typical dynamical behavior characterized by a decay from a value M^{2N} reaching a dip after $m \approx \sqrt{M}$ iterations of the Floquet operator. Finally, the SFF reaches a plateau at $m \sim M$ with a value NM^N that defines the long-time asymptote [20]. As expected, the SFF reaches a plateau at a time that scales with M as our estimate τ_H . Fig. 4 shows the long-time dynamics of the SFF $\mathcal{R}_2(mT)$ [see Eq. (13)] in the single-particle sector.

In the regular regime [see Fig. 4(a)] the SFF displays a dip, but not a pronounced ramp before reaching the plateau. This indicates, along with the quasienergy statistics in Fig. 3(b), that in this region the system is not chaotic. We will later show that in this region the system may not be complex enough for boson sampling to be hard. In the chaotic regions [see Fig. 4(c)(d)] the SFF displays the typical features associated with systems that exhibit QSOC. However, even in the crossover region [see Fig. 4(b)] there are weak QSOC, exhibiting a dip, ramp, and plateau. But, as we will show in Section VIII D, in the crossover regime the system may not have complex random Gaussian submatrices.

C. Long-time dynamics of local observables

In this section we will show numerical evidence of the dynamics of $\langle \hat{n}_l(mT) \rangle$ and the probability $P_F(mT)$ for our photonic circuit with $N = 2$ photons in $M = 12$ modes. In this case, the single-particle unitary can be represented as a 12×12 unitary matrix $U_S(mT)$. This is an interesting example, as the system has a small system size far away of the semiclassical regime $M \gg 1$.

In Fig. 5 we plot the stroboscopic dynamics of $\langle \hat{n}_l(mT) \rangle$ in the regular regime for $N = 2$ photons. From this one can see that the photons remain localized and there are regions of the chain that cannot be accessed as we show in Fig. 5 a). On the contrary, when the system approaches the chaotic regime, it can explore more modes along the lattice, as we show in Fig. 5 b). To benchmark our results, Fig. 5 c) depict the dynamics of the local mean number of photons when the evolution operator is a random matrix drawn from the circular unitary ensemble (CUE) [31, 41]. When our system approaches the chaotic regime, the dynamics is very close to the case of a random matrix as can be seen in Fig. 5. In these numerical results, we show the dynamics during $m \approx M = 12$ periods, which is close to the time scale required to reach the Plateau of the SFF in Fig. 4.

Next it is illustrative to investigate the populations $P_F(mT)$ of the different configurations. The dynamics of multiple photons can be interpreted as a quantum walk in the Hilbert space [87]. In Fig. 5 (d) and (e) we plot the time evolution of the probabilities $P_F(mT) = |\gamma_F(mT)|^2$ in the regular and chaotic regimes. For comparison Fig. 5 f) shows the dynamics of $P_F(mT)$ for a random matrix drawn from CUE.

The results presented so far show that single-particle QSOC lead to equilibration of observables. We also show the intimate relation between spectral statistics, spectral form factors and photonic OTOCs and discuss the role that they play on the dynamics. However, these arguments still do not show if chaotic systems provide the complexity required to perform boson sampling. We address this in the next section.

D. Statistical properties of submatrices and complexity of boson sampling

At the single-particle level, and as we can see from Eq. (16), a regular system cannot effectively explore all the modes M of the chain because the transition probability, $U_{i,r}(mT) = \langle i|U(mT)|r \rangle$, between two modes depends on the localization properties of the wave functions. Furthermore, it is also restricted by conservation laws. However, when the system enters the ergodic regime these constraints disappear due to perturbations that break the regular motion [87], and the system is able to explore more configurations [79, 88]. From this it follows that when the disorder is weak and θ is chosen such that the system exhibits GOE statistics [see Fig. 3], the operator spreading shows a linear light cone. As we discussed in Section III, when the disorder is strong the photons are localized and the operator spreading exhibits a logarithmic light cone.

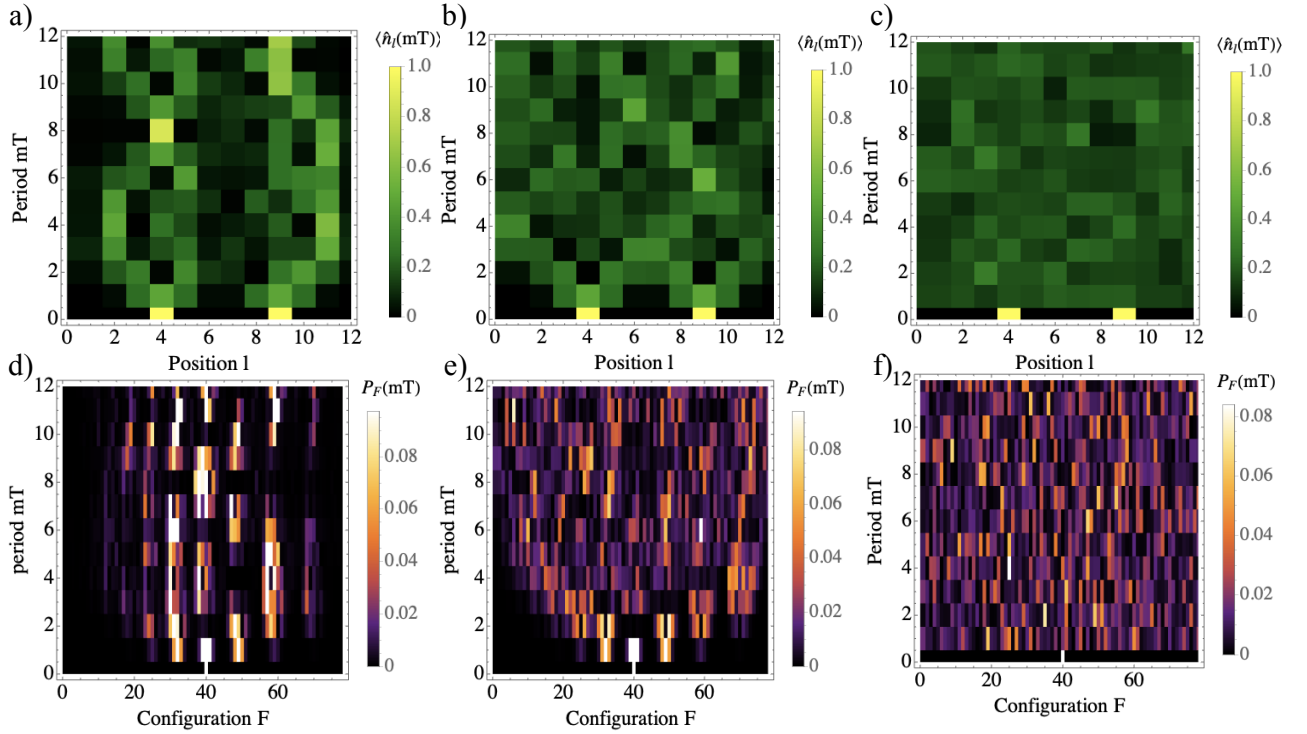


FIG. 5. Dynamics over $m = 12$ cycles for $N = 2$ photons in $M = 12$ modes for a single realization of disorder. *a)* ($W = 7/16\Phi$) and *b)* ($W = 1/8\Phi$) depict the dynamics of the mean number of photons $\langle \hat{n}_l(mT) \rangle$ for regular and chaotic unitaries, respectively. *d)*, *e)* show $P_F(mT)$ for regular and chaotic unitaries, respectively. Clearly, in the regular regime, the system only explores a small portion of the available configurations. We benchmark our results using the a unitary evolution drawn from the Haar measure in *c)* and *f)*. The dynamics in *a)* and *b)* resemble the light cone structure illustrated in Fig. 1. For the simulation we set $\Phi = \pi/4$ and $\theta = 7.4/16\Theta$.

When the system exhibits QSOC we expect the elements of the single-particle unitary to be independent complex random Gaussian variables $U_{ij}(mT) \sim Z = X + iY$, where X and Y are independent real random Gaussian variables with means $E(X) = E(Y) = 0$ and variances $E(X^2) = E(Y^2) = \sigma/2$. For boson sampling it is sufficient that the elements of the top left $N \times N$ submatrix are close in variation distance to complex random Gaussian variables [41]. In order to determine this for the kicked rotor, we consider boson sampling with $N = 5$ photons in $M = 300$ modes. The photons are initialized in the first five modes, $i = 1, \dots, 5$, and measured at the output in modes $j = 1, \dots, 5$. We take as a probability sample the real and imaginary parts of the elements of $U_{ij}(mT)$ from $|\mathcal{E}_U| = 100$ disorder realizations.

In Fig. 6 we show the probability distribution of the elements after $m = 300$ cycles. In the regular regime [see Fig. 6(a)] the probability distribution is not Gaussian. This is because the single-photon dynamics are localized, and even at long times ($m \sim M$) the evolution will not have the required complexity. In contrast, when the system exhibits QSOC the probability distribution appears Gaussian [see Fig. 6(c)-(d)], because the operator spreading exhibits a linear light cone and the photons explore all modes of the chain. In the crossover regime [see Fig. 6(b)] the elements also appear Gaussian, but a more careful examination will show that the distribution deviates.

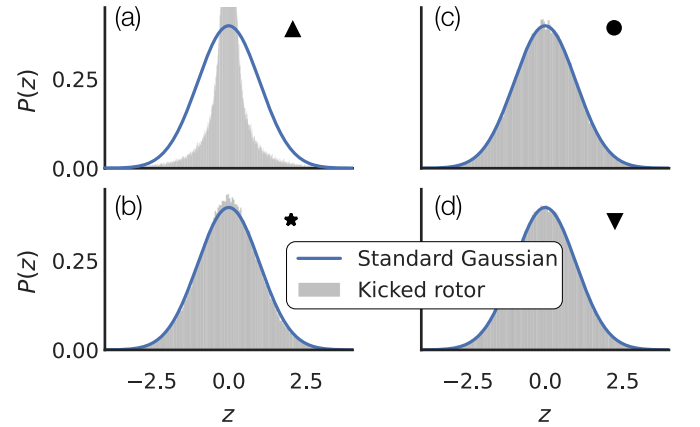


FIG. 6. Probability densities of the complex elements of a 5×5 submatrix of the kicked rotor after $m = 300$ cycles, standardized to the standard Gaussian distribution. The upwards triangle, star, circle, and downwards triangle correspond to subfigures in Fig. 3. Calculated for $|\mathcal{E}_U| = 100$ disorder realizations and $M = 300$ modes.

A useful way to compare two probability distributions in a graphical fashion is to use a quantile-quantile (Q-Q) plot [89]. A typical Q-Q plot is a parametric curve where one of the quantiles of one distribution is plotted against the same quantile of another distribution. In Fig. 7 we show a Q-Q plot

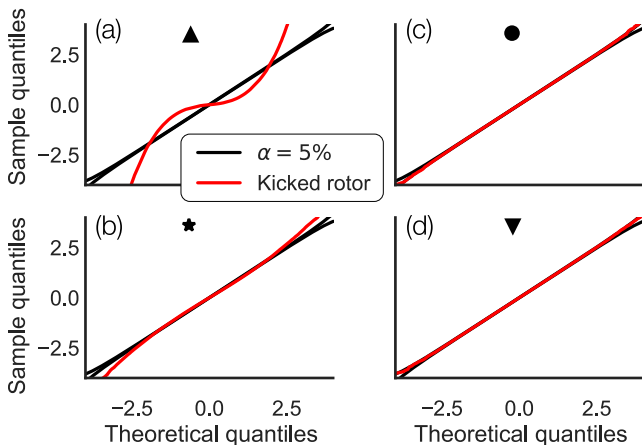


FIG. 7. Q-Q plot comparing against a theoretical Gaussian distribution of the complex elements of a 5×5 submatrix of the kicked rotor ($N = 5$ photons in $M = 300$ modes) after $m = 300$ cycles. When the spectral statistics are (a) Poissonian the distribution does not lie on a straight line and is not Gaussian. In the regime where there are QSOC (c)-(d) the distribution is approximately Gaussian. In the crossover regime (b) the distribution has light tails and is not a Gaussian distribution to within a $\alpha = 5\%$ significance level. The upwards triangle, star, circle, and downwards triangle correspond to subfigures in Fig. 3.

against a theoretical Gaussian distribution. If the elements are complex random Gaussian variables then the points will approximately lie on a straight line. This is the case for when the kicked rotor exhibits QSOC [see Fig. 7(c)-(d)]. We see that in the crossover regime that the tails of the distribution are light and deviate from a Gaussian distribution [see Fig. 7(b)]. We have further confirmed that in the crossover the distribution deviates from a Gaussian by using a Shapiro–Wilk test for normality [90] with an $\alpha = 5\%$ significance level.

We wish to highlight that the conclusions from our results do not change for long times well past the Heisenberg time τ_H . Furthermore, we have confirmed that our results are unchanged for submatrices of sizes $N = 2, \dots, 30$.

IX. CONCLUSIONS

In their original paper [41], Aaronson and Arkhipov show that a unitary from the CUE will be sufficient for boson sampling to be hard. In our work, we have shown that one can perform boson sampling exploiting the time evolution of a system that exhibits QSOC and that this will also be hard, because the dynamics is linked to operator spreading and how well a single photon delocalizes across all modes of the system. Hence, we argue that any photonic system that exhibits QSOC should be a hard boson sampling task. As we proposed, this can be explored in the disordered quantum kicked rotor using waveguides in periodic photonic chips.

Of course, our test that the elements are approximately Gaussian may be too strict. We have not quantified the total variation distance to a Gaussian distribution for boson sam-

pling to be hard. It is possible that even in the crossover regime, where the QSOC are weak, that the distribution is sufficiently approximately Gaussian. Specifically, in the crossover regime the maximum deviation of the distribution occurs at the tails. A route to resolve this may be to consider the empirical cumulative distribution function and connect it to the total variation distance measure that relates the hardness of boson sampling with the Permanent-of-Gaussians Conjecture [41] for a given number of modes, M , and particles, N .

In future works, it would be interesting to explore how to use ideas of condensed matter physics to further break symmetries of the unitary. For example, this may allow one to explore chaotic systems with CUE spectral statistics by breaking time reversal symmetries. In real implementations, the photonic system is affected by photon loss. Therefore, a natural question is to explore how these loss mechanism affects the chaotic dynamics in our photonic implementation. In our work, we presented numerical calculations showing that in some regimes, submatrices of the unitary show Gaussian statistics. It would be useful to find an analytical proof of this by using tools of QSOC.

Acknowledgments.— V. M. Bastidas thanks M. M. Zapata-Alvarez and valuable discussions with K. Azuma, H. W. Lau, L. Ruks, and H. Takesue. The authors acknowledge partial support through the MEXT Quantum Leap Flagship Program (MEXT Q-LEAP) under Grant No. JPMXS0118069605.

Appendix A: Calculation of time averages

The purpose of this appendix is to provide a formal derivation of the time average of observables. This type of averages plays a very important role in describing equilibration in periodically-driven quantum system provided that the quasienergies show level repulsion.

1. Formal derivation of time averages

Let us consider the regime $M \gg 1$ of time averages such as the one in Eqs. (28) and (32). These averages contain quantities of the generic form

$$\bar{Q}_{2N} = \frac{1}{\mathcal{M}} \sum_{m=0}^{M-1} e^{-i(\sum_{\epsilon \in \zeta} \xi_{\zeta} - \sum_{\eta \in \eta} \xi_{\eta})mT/\hbar}, \quad (\text{A1})$$

where $\zeta = (\zeta_1, \zeta_2, \dots, \zeta_N)$ and $\eta = (\eta_1, \eta_2, \dots, \eta_N)$. It is instructive to see the explicit expressions for $N = 1$ and $N = 2$

$$\begin{aligned} \bar{Q}_2 &= \frac{1}{\mathcal{M}} \sum_{m=0}^{M-1} e^{-i(\xi_{\alpha} - \xi_{\beta})mT/\hbar} \\ \bar{Q}_4 &= \frac{1}{\mathcal{M}} \sum_{m=0}^{M-1} e^{-i(\xi_{\alpha} + \xi_{\lambda} - \xi_{\beta} - \xi_{\rho})mT/\hbar}. \end{aligned} \quad (\text{A2})$$

To calculate this type of averages in a formal way, it is useful to perform the sums explicitly. With this in mind, we consider

a generic power series as follows

$$F(\phi - z) = \frac{1}{\mathcal{M}} \sum_{m=0}^{\mathcal{M}-1} e^{-im(\phi-z)} = \frac{1 - e^{i(z-\phi)\mathcal{M}}}{\mathcal{M}(1 - e^{i(z-\phi)})}$$

$$= \left(\frac{1 - e^{i(z-\phi)\mathcal{M}}}{\mathcal{M}} \right) \sum_{l=0}^{\infty} \frac{i^{l-1} B_l}{l!} (z - \phi)^{l-1}. \quad (\text{A3})$$

where ϕ is a real variable and $z = z_R + iz_I$ with $z_I \geq 0$ is a complex number added for convergence of the series. In this derivation, we also have used the generating function of the B_l the Bernoulli numbers [75]

$$\frac{1}{1 - e^{i(z-\phi)}} = \sum_{l=0}^{\infty} \frac{i^{l-1} B_l}{l!} (z - \phi)^{l-1} \quad (\text{A4})$$

Next, let us carefully investigate the convergence of the power series in Eq. (A3) in the complex plane. As a first step, we can notice that $F(0) = 1$ when $z = \phi$. The second step is to look at the series far from the point $z = \phi$ defining a scale $R = |z - \phi|^{-1}$. Due to the exponential decay $e^{-z_I \mathcal{M}}$, the exponential term in Eq. (A3) vanishes for $\mathcal{M} \gg R$ provided that $|z - \phi| \neq 0$. By using this, we can obtain the bound

$$|F(1/R)| \leq \frac{1}{\mathcal{M}} \sum_{l=0}^{\infty} \frac{i^{l-1} B_l}{l!} R^{1-l}. \quad (\text{A5})$$

This clearly tends to zero when $\mathcal{M} \gg R$. The trick to calculate the average is to take the limit $|z| \rightarrow 0$. This allows us to approach the resonance condition $\phi = 0$ in the complex plane. After taking the limit $|z| \rightarrow 0$, we define a real function $F(\phi)$, from the previous discussion, we know that $F(\phi) = 1$ if $\phi = 0$ and $F(\phi) = 0$ when $\phi \neq 0$. Keeping this in mind, we obtain

$$\bar{Q}_2 = \delta_{\alpha,\beta}$$

$$\bar{Q}_4 = \delta_{\alpha,\beta} \delta_{\lambda,\rho} + \delta_{\alpha,\rho} \delta_{\lambda,\beta}. \quad (\text{A6})$$

The first expression follows from the generic Floquet spectrum [13] by setting $\phi = (\xi_\alpha - \xi_\beta)T/\hbar = T/\tau_{\alpha,\beta}$. From this equation, it is clear the meaning of the scale $R = \tau_{\alpha,\beta}/T$ that tells us how many periods we need to wait to obtain a well-defined time average, as we discussed in the main text. To obtain the second equation, we need to be careful because $\phi = (\xi_\alpha + \xi_\lambda - \xi_\beta - \xi_\rho)T/\hbar$. Thus, we can have a resonance $\alpha = \beta$ and an effective scale $R = \tau_{\lambda,\rho}/T$. Alternatively, we can have $\lambda = \rho$ and $R = \tau_{\alpha,\beta}/T$. For this reason, we need to take care of the possible combinations defining the time scales $\mathcal{M} \gg R$ to perform the time average. The averages discussed here resemble the results for time-independent systems in Ref. [82]. To calculate the general time average in Eq. (12), one needs to consider all the possible pairs for which one reaches the resonance $\xi_\zeta - \xi_\eta$ for $\zeta \in \zeta$ and $\eta \in \eta$. For the general expression of this time average, we refer the reader to Appendix C4 of Ref. [13].

2. Time averages and Floquet generalized Gibbs states

Let us explain in detail what is the nature of time averages of local observables. With this aim, we investigate what happens with the dynamics of a single particle initialized in the

state $|\psi(0)\rangle = \hat{a}_i^\dagger |0\rangle$ in the chaotic regime. After m periods of the circuit, the evolution of the particle is given by

$$|\psi(mT)\rangle = \sum_{\alpha} e^{-i\xi_\alpha mT/\hbar} c_{i,\alpha} |\alpha\rangle. \quad (\text{A7})$$

To investigate thermalization in quadratic Hamiltonians [82], it is useful to define the time average of a single-particle observable \hat{O} . One example of this is $\hat{O} = \hat{n}_i$. The time-averaged expectation value of such a single-particle observable over a total number \mathcal{M} of periods of the drive is given by

$$\bar{O} = \frac{1}{\mathcal{M}} \sum_{m=0}^{\mathcal{M}-1} \langle \hat{O}(mT) \rangle =$$

$$= \frac{1}{\mathcal{M}} \sum_{m=0}^{\mathcal{M}-1} \sum_{\alpha,\beta} e^{-i(\xi_\alpha - \xi_\beta)mT/\hbar} c_{i,\alpha} c_{i,\beta}^* \langle \beta | \hat{O} | \alpha \rangle. \quad (\text{A8})$$

From this expression, we clearly see the relation to \bar{Q}_2 in Eq. (A1). In the last section, we obtained the average $\bar{Q}_2 = \delta_{\alpha,\beta}$, which give us the time average

$$\bar{O} = \sum_{\alpha} |c_{i,\alpha}|^2 \langle \alpha | \hat{O} | \alpha \rangle = \text{tr}(\hat{\rho}_{\text{GGE}} \hat{O}), \quad (\text{A9})$$

where

$$\hat{\rho}_{\text{GGE}} = \sum_{\alpha} |\alpha\rangle\langle\alpha| e^{-\Gamma_\alpha \xi_\alpha} / Z, \quad (\text{A10})$$

is a density matrix representing the Floquet generalized Gibbs ensemble [77]. Here $\Gamma_\alpha = 1/k_B T_\alpha$ and T_α are effective temperatures determined by the conserved quantities, while Z is a normalization constant [77]. The direct implication of this is that due to level repulsion, the weights satisfy the relation $|c_{i,\alpha}|^2 \approx e^{-\Gamma_\alpha \xi_\alpha} / Z$ that we used in the main text.

Appendix B: Connection to the kicked rotor

In this section we show that a classical limit of Eq. (43) at the single-particle level realizes a kicked rotor [50–56], which is an archetypal model for chaos. Hence, we will show that the growth in complexity of Eq. (43) (see Figs. 3,4) is associated with the destruction of quasi-periodic orbits and a transition to the chaotic regime of a classical Hamiltonian

1. Semiclassical Hamiltonian in the absence of disorder ($W = 0$)

It is useful to consider periodic boundaries $\hat{a}_{M+1} = \hat{a}_1$ and transform to the reciprocal lattice with the discrete Fourier transform

$$\hat{A}_k \equiv \frac{1}{\sqrt{M}} \sum_{j=1}^M e^{-ibkj} \hat{a}_j, \quad (\text{B1})$$

where k labels the crystal momentum and we set the lattice constant $b = 1$. In this case, the variable k is discrete and satisfies the condition $k = 2s\pi/M$ with integer s . Importantly, for

a finite chain, the values of k are restricted to the first Brillouin zone $-\pi \leq k \leq \pi - 2\pi/M$. Using the identity

$$\frac{1}{M} \sum_j e^{-i(k_2-k_1)j} = \delta_{k_1, k_2}, \quad (\text{B2})$$

where δ_{k_1, k_2} is the Kronecker delta function, Eq. (43) becomes

$$\begin{aligned} \hat{H}(t) = & \frac{1}{M} \sum_{j, k_1, k_2} \frac{\hbar \phi_j}{T} e^{-i(k_1-k_2)j} \hat{A}_{k_1}^\dagger \hat{A}_{k_2} \\ & + 2\hbar J(t) \sum_k \cos(k_1) \hat{A}_k^\dagger \hat{A}_k, \end{aligned} \quad (\text{B3})$$

where $J(t) = \frac{\theta}{T} \sum_{m=-\infty}^{\infty} \delta(t/T - m)$. Since Eq. (43) is quadratic we may restrict our analysis to the single-particle subspace.

A general single-particle state in the reciprocal lattice basis is given by

$$|\psi(t)\rangle \equiv \sum_k \psi_k(t) \hat{A}_k^\dagger |0\rangle, \quad (\text{B4})$$

where $\hat{A}_k |0\rangle = 0$ defines the vacuum $|0\rangle$ and $\psi_k(t)$ is a complex coefficient. The time-dependent Schrödinger equation $i\hbar \partial_t |\psi(t)\rangle = \hat{H}(t) |\psi(t)\rangle$ is given by

$$\begin{aligned} \sum_k i\hbar \partial_t \psi_k(t) \hat{A}_k^\dagger |0\rangle = & \frac{1}{M} \sum_{j, k, k_1} \frac{\hbar \phi_j}{T} e^{-i(k_1-k)j} \psi_{k_1}(t) \hat{A}_k^\dagger |0\rangle \\ & + 2\hbar J(t) \sum_k \cos(k) \psi_k(t) \hat{A}_k^\dagger |0\rangle, \end{aligned} \quad (\text{B5})$$

where we used the commutation relation $[A_{k_1}, A_{k_2}^\dagger] = \delta_{k_1, k_2}$ for bosons. Eq. (B5) defines an equation of motion for the coefficients $\psi_k(t)$, given by

$$\hbar \partial_t \psi_k(t) = \frac{1}{M} \sum_{j, k_1} \frac{\hbar \phi_j}{T} e^{-i(k_1-k)j} \psi_{k_1}(t) + 2\hbar J(t) \cos(k) \psi_k(t). \quad (\text{B6})$$

To obtain the semiclassical Hamiltonian, it is useful to calculate the following expression

$$\sum_{j, k_2} \frac{j e^{-i(k_1-k_2)j}}{M^2} \psi_{k_2}(t) = \lim_{\epsilon \rightarrow 0} \frac{i}{M^2} \sum_{j, k_2} \frac{e^{-i(k_1-k_2)j} (e^{-i\epsilon j} - 1)}{\epsilon} \psi_{k_2}(t). \quad (\text{B7})$$

To be mathematically precise, the right hand side of this equation can be interpreted as the derivative of the function

$$g(\epsilon) = \sum_{j, k_2} \frac{e^{-i(k_1-k_2+\epsilon)j}}{M^2} \psi_{k_2}(t) = \sum_{k_2} \left[\frac{e^{i\epsilon} - e^{-i\epsilon M}}{e^{i\epsilon} - e^{-i(k_1-k_2)}} \right] \frac{\psi_{k_2}(t)}{M^2} \quad (\text{B8})$$

with respect to ϵ and evaluated at $\epsilon = 0$ as follows

$$i \frac{dg(\epsilon)}{d\epsilon} \Big|_{\epsilon=0} = \sum_{j, k_2} \frac{j e^{-i(k_1-k_2)j}}{M^2} \psi_{k_2}(t). \quad (\text{B9})$$

So far all the calculations are exact. But now we will carefully look at Eqs. (B7) and (B8) in the large-volume limit $M \gg 1$ and make some approximations. As a first step, approximate the discrete sums in Eq. (B8) using an integral in the limit $M \gg 1$ as follow

$$\begin{aligned} g(\epsilon) = & \frac{1}{M} \sum_{k_2} \frac{1}{M \bar{\Delta}_k} \left[\frac{e^{i\epsilon} - e^{-i\epsilon M}}{e^{i\epsilon} - e^{-i(k_1-k_2)}} \right] \psi_{k_2}(t) \bar{\Delta}_k \\ \approx & \frac{1}{M} \int_{-\pi}^{\pi} \delta(k_1 - k_2 + \epsilon) \psi(k_2, t) dk_2 = \frac{\psi(k_1 + \epsilon, t)}{M}, \end{aligned} \quad (\text{B10})$$

where we defined $\psi(k, t)$ as the continuous version of $\psi_k(t)$. We also considered the volume element in the reciprocal space $\Delta_k = 2\pi/M$ and approximate the integrand Kernel by using a Dirac delta $\delta(k_1 - k_2 + \epsilon)$ in the limit $M \gg 1$ when $\Delta_k \rightarrow 0$. In the last derivation, we approximated the discrete sums using an integral in the limit $M \gg 1$ as follows

$$\sum_k f(k) = \frac{1}{\bar{\Delta}_k} \sum_k f(k) \bar{\Delta}_k \approx \frac{M}{2\pi} \int_{-\pi}^{\pi} f(k) dk. \quad (\text{B11})$$

This procedure allows us to approximate the sum in Eq. (B7) in terms of a scaled derivative of the wave function $\psi(k_1, t)$ as follows

$$\begin{aligned} \sum_{j, k_2} \frac{j e^{-i(k_1-k_2)j}}{M^2} \psi_{k_2}(t) \approx & \lim_{\epsilon \rightarrow 0} \frac{i}{M} \frac{\psi(k_1 + \epsilon, t) - \psi(k_1, t)}{\epsilon} \\ \approx & \frac{i \partial_{k_1} \psi(k_1, t)}{M}, \end{aligned} \quad (\text{B12})$$

where used $\psi(k_1 + \epsilon, t) \approx \psi(k_1, t) + \epsilon \partial_{k_1} \psi(k_1, t)$.

Hence, by using Eq. (B12) we can approximate the sum in Eq. (B6) as follows

$$\frac{1}{M} \sum_{j, k_1} \frac{\hbar \phi_j}{T} e^{-i(k_1-k)j} \psi_{k_1}(t) \approx \frac{4\hbar\Phi}{T} \left(\frac{i\partial_k}{M} - \frac{1}{2} \right)^2 \psi_k(t). \quad (\text{B13})$$

Defining the position as $\hat{q} \equiv b\hat{x} \equiv i\partial_k/M$ and momentum as $\hat{p} \equiv \hbar k/b$ (keeping in mind that $b = 1$), we recover the canonical commutation relation $[\hat{q}, \hat{p}] = i\hbar_{\text{eff}}$, with effective Planck constant $\hbar_{\text{eff}} \equiv \hbar/M$. Hence, for $M \gg 1$, position and momentum behave like commuting classical variables and may be replaced with real numbers $\hat{x} \rightarrow x$. In this limit we obtain the classical Hamiltonian

$$\begin{aligned} \mathcal{H}_C(k, x, t) = & \frac{4\hbar\Phi}{T} \left(x - \frac{1}{2} \right)^2 + 2\hbar J(t) \cos(k) \\ = & \frac{4\hbar\Phi}{T} \left(x - \frac{1}{2} \right)^2 + \frac{2\hbar\theta}{T} \cos(k) \sum_{m=-\infty}^{\infty} \delta(t/T - m), \end{aligned} \quad (\text{B14})$$

where (k, x) are classical canonical variables in phase space.

Next, let us calculate the classical equations of motion for

the Hamiltonian given by Eq. (B14)

$$\begin{aligned}\frac{\partial x}{\partial t} &= \frac{\partial \mathcal{H}(x, k, t)}{\hbar \partial k} = -\frac{2\theta}{T} \sin(k) \sum_{m=-\infty}^{\infty} \delta(t/T - m) \\ \hbar \frac{\partial k}{\partial t} &= -\frac{\partial \mathcal{H}(x, k, t)}{\partial x} = -\frac{8\hbar\Phi}{T} \left(x - \frac{1}{2}\right).\end{aligned}\quad (\text{B15})$$

The integration of the equations of motion during a period T of the drive gives us a discrete map that give us the dynamics at stroboscopic times

$$\begin{aligned}x_{n+1} &= x_n - 2\theta \sin(k_n) \\ k_{n+1} &= k_n - 8\Phi \left(x_{n+1} - \frac{1}{2}\right).\end{aligned}\quad (\text{B16})$$

Next, let us define the new coordinate $X_n = -8\Phi \left(x_n - \frac{1}{2}\right)$ in such a way that the equations of motion for this new variables are given by

$$\begin{aligned}X_{n+1} &= X_n + \bar{K} \sin(k_n) \\ k_{n+1} &= k_n + X_{n+1},\end{aligned}\quad (\text{B17})$$

where $\bar{K} = 16\theta\Phi$.

2. Discussion about the relation to the Kicked rotor

One can identify Eq. (B14) with the model of a kicked rotor [50–56] with $x - 1/2 \rightarrow p$ playing the role of the momen-

tum and $k \rightarrow \theta$ the phase. Eq. (B14) can be written as

$$\mathcal{H}(\theta, p, t) = \frac{p^2}{2I} + K \cos \Theta \sum_{m=-\infty}^{\infty} \delta(t/T - m), \quad (\text{B18})$$

where $I = T/(8\hbar\Phi)$ is the moment of inertia and $K = 2\hbar\theta/T$ is the kicking strength. After integrating the equations of motions one obtains the discrete Chirikov map

$$\begin{aligned}P_{n+1} &= P_n + \bar{K} \sin \Theta_n \\ \Theta_{n+1} &= \Theta_n + P_{n+1},\end{aligned}\quad (\text{B19})$$

where the angular momentum is $P \equiv pT/I$ and the renormalized kicking strength is $\bar{K} \equiv KT^2/I = 16\theta\Phi$ as defined previously.

The equations of motion of Eq. (B18) depend on a single parameter \bar{K} . It has the same structure as the kicked rotor conventionally found in textbooks, but the topology of the phase space differs. In a conventional kicked rotor the phase space lives on a torus because P_n is taken modulo 2π . In the kicked rotor defined by Eq. (B18), the domain of P_n is any real number and hence the topology of the phase space is a cylinder.

Hence, we can identify the classical limit of Eq. (43) with the dynamics of the kicked rotor. When $\bar{K} = 0$ the dynamics is regular and the system shows only periodic orbits. The delta kicks proportional to \bar{K} break the periodic orbits inducing a transition to chaos. For example, for $\bar{K} = 4$, the system shows a mixed phase space with regular islands. The latter are completely absent when $\bar{K} = 7$ and the system is fully chaotic.

Some comments about the topology of the phase space and the definition of the coordinates X_n and k_n in Eq. (B17) are in order. In the derivation of the semiclassical limit we have assumed periodic boundary conditions such that the position is in the domain $0 \leq x_n < 1$ and the momentum naturally is restricted to $-\pi < k_n < \pi$. Topologically, this defines a torus. Consequently, the rescaled coordinates are defined in the domain $-4\Phi \leq X_n < 4\Phi$ and $-\pi < k_n < \pi$.

-
- [1] P. Stavroulakis, *Chaos applications in telecommunications* (CRC press, 2005).
- [2] G. Chen and X. Yu, *Chaos control: theory and applications*, Vol. 292 (Springer Science & Business Media, 2003).
- [3] E. N. Lorenz, *J. Atmos. Sci.* **20**, 130 (1963).
- [4] J. P. Eckmann and D. Ruelle, *Rev. Mod. Phys.* **57**, 617 (1985).
- [5] A. Trevisan and L. Palatella, *Int. J. Bifurc. Chaos Appl. Sci. Eng.* **21**, 3389 (2011).
- [6] A.-L. Chian, F. Borotto, T. Hada, R. Miranda, P. Munoz, and E. Rempel, *Rev. Mod. Plasma Phys.* **6**, 1 (2022).
- [7] W.-C. Chen, *Chaos, Solitons & Fractals* **36**, 1305 (2008).
- [8] H.-J. Stöckmann and J. Stein, *Phys. Rev. Lett.* **64**, 2215 (1990).
- [9] F. Haake, *Quantum signatures of chaos*, 3rd ed., Springer Series in Synergetics (Springer, Berlin, Germany, 2010).
- [10] E. Stechel and E. Heller, *Annu. Rev. Phys. Chem.* **35**, 563 (1984).
- [11] J. K. Breslin, C. A. Holmes, and G. J. Milburn, *Phys. Rev. A* **56**, 3022 (1997).
- [12] R. Jalabert, J.-L. Pichard, and C. Beenakker, *Europhys. Lett.* **27**, 255 (1994).
- [13] L. Leone, S. F. E. Oliviero, and A. Hamma, *Entropy* **23** (2021).
- [14] S. F. E. Oliviero, L. Leone, F. Caravelli, and A. Hamma, *SciPost Phys.* **10**, 076 (2021).
- [15] D. Delande and J. C. Gay, *Phys. Rev. Lett.* **57**, 2006 (1986).
- [16] M. Hentschel and K. Richter, *Phys. Rev. E* **66**, 056207 (2002).
- [17] M. Gutiérrez and A. Goussev, *Phys. Rev. E* **79**, 046211 (2009).
- [18] B. Yan, L. Cincio, and W. H. Zurek, *Phys. Rev. Lett.* **124**, 160603 (2020).
- [19] D. A. Roberts and B. Yoshida, *Journal of High Energy Physics* **2017**, 121 (2017).
- [20] J. Cotler, N. Hunter-Jones, J. Liu, and B. Yoshida, *J. High Energy Phys.* **2017** (11), 48.
- [21] J. Rammensee, J. D. Urbina, and K. Richter, *Phys. Rev. Lett.* **121**, 124101 (2018).
- [22] H. Shen, P. Zhang, Y.-Z. You, and H. Zhai, *Phys. Rev. Lett.* **124**, 200504 (2020).
- [23] X. Mi, P. Roushan, C. Quintana, S. Mandra, J. Marshall, C. Neill, F. Arute, K. Arya, J. Atalaya, R. Babbush, *et al.*, *Sci-*

- ence **374**, 1479 (2021).
- [24] A. Sahu, N. D. Varikuti, and V. Madhok, arXiv:2211.11221 (2022).
- [25] J. Harris, B. Yan, and N. A. Sinitsyn, *Phys. Rev. Lett.* **129**, 050602 (2022).
- [26] O. Bohigas, M. J. Giannoni, and C. Schmit, *Phys. Rev. Lett.* **52**, 1 (1984).
- [27] M. V. Berry, *Proceedings of the Royal Society of London. A. Mathematical and Physical Sciences* **400**, 229 (1985).
- [28] K. Richter and M. Sieber, *Phys. Rev. Lett.* **89**, 206801 (2002).
- [29] S. Müller, S. Heusler, P. Braun, F. Haake, and A. Altland, *Phys. Rev. Lett.* **93**, 014103 (2004).
- [30] C. W. J. Beenakker, *Rev. Mod. Phys.* **69**, 731 (1997).
- [31] T. Guhr, A. Müller-Groeling, and H. A. Weidenmüller, *Phys. Rep.* **299**, 189 (1998).
- [32] G. E. Mitchell, A. Richter, and H. A. Weidenmüller, *Rev. Mod. Phys.* **82**, 2845 (2010).
- [33] F. L. Moore, J. C. Robinson, C. Bharucha, P. E. Williams, and M. G. Raizen, *Phys. Rev. Lett.* **73**, 2974 (1994).
- [34] F. L. Moore, J. C. Robinson, C. F. Bharucha, B. Sundaram, and M. G. Raizen, *Phys. Rev. Lett.* **75**, 4598 (1995).
- [35] K. A. Landsman, C. Figgatt, T. Schuster, N. M. Linke, B. Yoshida, N. Y. Yao, and C. Monroe, *Nature* **567**, 61 (2019).
- [36] P. Roushan, C. Neill, J. Tangpanitanon, V. M. Bastidas, A. Megrant, R. Barends, Y. Chen, Z. Chen, B. Chiaro, A. Dunsworth, *et al.*, *Science* **358**, 1175 (2017).
- [37] C. Zha, V. M. Bastidas, M. Gong, Y. Wu, H. Rong, R. Yang, Y. Ye, S. Li, Q. Zhu, S. Wang, Zhao, *et al.*, *Phys. Rev. Lett.* **125**, 170503 (2020).
- [38] E. R. Caianiello, *Nuovo Cim* **10**, 1634 (1953).
- [39] L. G. Valiant, *Theoretical computer science* **8**, 189 (1979).
- [40] L. Troyansky and N. Tishby, *Proc. Phys. Comput*, 96 (1996).
- [41] S. Aaronson and A. Arkhipov, in *Proc. Annu. ACM Symp. Theory Comput.* (2011) pp. 333–342.
- [42] D. J. Brod, E. F. Galvão, A. Crespi, R. Osellame, N. Spagnolo, and F. Sciarrino, *Advanced Photonics* **1**, 034001 (2019).
- [43] D. Hangleiter and J. Eisert, *Rev. Mod. Phys.* **95**, 035001 (2023).
- [44] M. C. Tichy, M. Tiersch, F. Mintert, and A. Buchleitner, *New Journal of Physics* **14**, 093015 (2012).
- [45] C. Dittel, G. Dufour, M. Walschaers, G. Weihs, A. Buchleitner, and R. Keil, *Phys. Rev. Lett.* **120**, 240404 (2018).
- [46] J. Carolan, J. D. Meinecke, P. J. Shadbolt, N. J. Russell, N. Ismail, K. Wörhoff, T. Rudolph, M. G. Thompson, J. L. O’Brien, J. C. Matthews, *et al.*, *Nature Photonics* **8**, 621 (2014).
- [47] N. J. Russell, L. Chakhmakhchyan, J. L. O’Brien, and A. Laing, *New journal of physics* **19**, 033007 (2017).
- [48] G. Muraleedharan, A. Miyake, and I. H. Deutsch, *New Journal of Physics* **21**, 055003 (2019).
- [49] A. Deshpande, B. Fefferman, M. C. Tran, M. Foss-Feig, and A. V. Gorshkov, *Phys. Rev. Lett.* **121**, 030501 (2018).
- [50] A. Altland and M. R. Zirnbauer, *Phys. Rev. Lett.* **77**, 4536 (1996).
- [51] H. Ammann, R. Gray, I. Shvarchuck, and N. Christensen, *Phys. Rev. Lett.* **80**, 4111 (1998).
- [52] M. B. d’Arcy, R. M. Godun, M. K. Oberthaler, D. Cassettari, and G. S. Summy, *Phys. Rev. Lett.* **87**, 074102 (2001).
- [53] A. Iomin, S. Fishman, and G. M. Zaslavsky, *Phys. Rev. E* **65**, 036215 (2002).
- [54] I. Manai, J.-F. m. c. Clément, R. Chicireanu, C. Hainaut, J. C. Garreau, P. Szriftgiser, and D. Delande, *Phys. Rev. Lett.* **115**, 240603 (2015).
- [55] P. Akridas-Morel, N. Cherroret, and D. Delande, *Phys. Rev. A* **100**, 043612 (2019).
- [56] M. Santhanam, S. Paul, and J. B. Kannan, *Physics Reports* **956**, 1 (2022).
- [57] P. Kok, W. J. Munro, K. Nemoto, T. C. Ralph, J. P. Dowling, and G. J. Milburn, *Rev. Mod. Phys.* **79**, 135 (2007).
- [58] M. Grifoni and P. Hänggi, *Physics Reports* **304**, 229 (1998).
- [59] M. C. Rechtsman, J. M. Zeuner, Y. Plotnik, Y. Lumer, D. Podolsky, F. Dreisow, S. Nolte, M. Segev, and A. Szameit, *Nature* **496**, 196 (2013).
- [60] B. T. Gard, K. R. Motes, J. P. Olson, P. P. Rohde, and J. P. Dowling, in *From atomic to mesoscale: The role of quantum coherence in systems of various complexities* (World Scientific, 2015) pp. 167–192.
- [61] T. F. See, V. M. Bastidas, J. Tangpanitanon, and D. G. Angelakis, *Phys. Rev. A* **99**, 033835 (2019).
- [62] H. Barghathi, J. Yu, and A. Del Maestro, *Phys. Rev. Res.* **2**, 043206 (2020).
- [63] F. Arute, K. Arya, R. Babbush, D. Bacon, J. C. Bardin, R. Barends, R. Biswas, S. Boixo, F. G. Brandao, D. A. Buell, *et al.*, *Nature* **574**, 505 (2019).
- [64] J. Tangpanitanon, S. Thanasilp, M.-A. Lemonde, N. Dangniam, and D. G. Angelakis, *Quantum Science and Technology* **8**, 025019 (2023).
- [65] M. Bukov, L. D’Alessio, and A. Polkovnikov, *Advances in Physics* **64**, 139 (2015).
- [66] V. Oganesyan and D. A. Huse, *Phys. Rev. B* **75**, 155111 (2007).
- [67] Y. Y. Atas, E. Bogomolny, O. Giraud, and G. Roux, *Phys. Rev. Lett.* **110**, 084101 (2013).
- [68] M. Srednicki, *Phys. Rev. E* **50**, 888 (1994).
- [69] F. Borgonovi, F. M. Izrailev, L. F. Santos, and V. G. Zelevinsky, *Physics Reports* **626**, 1 (2016).
- [70] C. Murthy and M. Srednicki, *Phys. Rev. Lett.* **123**, 230606 (2019).
- [71] A. Lazarides, A. Das, and R. Moessner, *Phys. Rev. Lett.* **115**, 030402 (2015).
- [72] M. Serbyn and J. E. Moore, *Phys. Rev. B* **93**, 041424 (2016).
- [73] P. Sierant and J. Zakrzewski, *Phys. Rev. B* **99**, 104205 (2019).
- [74] L. K. Joshi, A. Elben, A. Vikram, B. Vermersch, V. Galitski, and P. Zoller, *Phys. Rev. X* **12**, 011018 (2022).
- [75] I. S. Gradshteyn and I. M. Ryzhik, *Table of integrals, series, and products* (Academic press, 2014).
- [76] C. K. Burrell and T. J. Osborne, *Phys. Rev. Lett.* **99**, 167201 (2007).
- [77] T. Ishii, T. Kuwahara, T. Mori, and N. Hatano, *Phys. Rev. Lett.* **120**, 220602 (2018).
- [78] L. D’Alessio and M. Rigol, *Phys. Rev. X* **4**, 041048 (2014).
- [79] A. Haldar, R. Moessner, and A. Das, *Phys. Rev. B* **97**, 245122 (2018).
- [80] C. Fleckenstein and M. Bukov, *Phys. Rev. B* **103**, 144307 (2021).
- [81] F. Borgonovi and F. M. Izrailev, *Phys. Rev. E* **99**, 012115 (2019).
- [82] P. Łydzba, M. Mierzejewski, M. Rigol, and L. Vidmar, arXiv:2210.00016 (2022).
- [83] F. H. B. Somhorst, R. van der Meer, M. Correa Anguita, R. Schadow, H. J. Sniijders, M. de Goede, B. Kassenberg, P. Venderbosch, C. Taballione, *et al.*, *Nat. Commun.* **14**, 3895 (2023).
- [84] J. B. Spring, B. J. Metcalf, P. C. Humphreys, W. S. Kolthammer, X.-M. Jin, M. Barbieri, A. Datta, N. Thomas-Peter, N. K. Langford, D. Kundys, *et al.*, *Science* **339**, 798 (2013).
- [85] M. Walschaers, J. Kuipers, J.-D. Urbina, K. Mayer, M. C. Tichy, K. Richter, and A. Buchleitner, *New Journal of Physics* **18**, 032001 (2016).
- [86] A. W. Glaetzle, K. Ender, D. S. Wild, S. Choi, H. Pichler, M. D. Lukin, and P. Zoller, *Phys. Rev. X* **7**, 031049 (2017).

- [87] M. P. Estarellas, T. Osada, V. M. Bastidas, B. Renoust, K. Sanaka, W. J. Munro, and K. Nemoto, *Sci. Adv.* **6**, eaay8892 (2020).
- [88] N. Regnault and R. Nandkishore, *Phys. Rev. B* **93**, 104203 (2016).
- [89] H. C. Thode, *Testing for normality* (Marcel Dekker, New York, 2002).
- [90] S. S. Shapiro and M. B. Wilk, *Biometrika* **52**, 591 (1965).